

Multi-decadal geomorphic changes of a low-angle valley glacier in East Kunlun Mountains: remote sensing observations and detachment hazard assessment

Xiaowen Wang^{1,2}, Lin Liu³, Yan Hu³, Tonghua Wu⁴, Lin Zhao^{4,5}, Qiao Liu⁶, Rui Zhang^{1,2}, Bo Zhang¹, Guoxiang Liu^{1,2}

¹Faculty of Geosciences and Environmental Engineering, Southwest Jiaotong University, China

5 ²State-Province Joint Engineering Laboratory of Spatial Information Technology of High-speed Rail Safety, Southwest Jiaotong University, China

³Earth System Science Programme, Faculty of Science, The Chinese University of Hong Kong, China

⁴Cryosphere Research Station on the Qinghai-Tibet Plateau, State Key Laboratory of Cryosphere Science, Northwest Institute of Eco-Environment and Resources, Chinese Academy of Sciences, China

10 ⁵School of Geographical Sciences, Nanjing University of Information Science and Technology, China

⁶Institute of Mountain Hazards and Environment, Chinese Academy of Sciences, China

Correspondence to: Xiaowen Wang (insarwxw@swjtu.edu.cn)

Abstract: Detachments of large parts of low-angle mountain glaciers in recent years have raised great attention due to their threats to lives and properties downstream. While current studies have mainly focused on post-event analysis, assessing the potential hazard of glaciers prone to detachment is rare. Here we presented a comprehensive analysis of the dynamics and runout hazard of a low-angle (~20°) valley glacier, close to the Qinghai-Tibet railway and highway, in the East Kunlun Mountains on the Qinghai-Tibet Plateau. The changes in morphology, terminus position, and surface elevation of the glacier between 1975 and 2021 were characterized with multi-sensor remote sensing data including a stereo-image pair from the historical KH-9 spy satellite, six Digital Elevation Models (DEMs), and eleven high-resolution images from Planet Labs. The surface flow velocities of the glacier tongue between 2009 and 2020 were also tracked based on cross-correlation of Planet images. Our observations show that the glacier snout has been progressively advancing in the past four decades, with a stepwise increase of advance velocity from $4.55 \pm 0.46 \text{ m} \cdot \text{a}^{-1}$ between 1975 and 2009 to $30.88 \pm 2.36 \text{ m} \cdot \text{a}^{-1}$ between 2015 and 2020. DEM differencing confirms the glacial advance, with surface thinning in the source region and thickening in the tongue. The net volume loss over the glacier tongue was about $11.21 \pm 2.66 \times 10^5 \text{ m}^3$ during 1975–2018. Image cross-correlation reveals that the surface flow velocity of the glacier tongue has been increasing in recent years, with the mean velocity below 4800 m more than tripled from $6.3 \pm 1.8 \text{ m} \cdot \text{a}^{-1}$ during 2009–2010 to $22.3 \pm 3.2 \text{ m} \cdot \text{a}^{-1}$ during 2019–2020. Piecing these observations together, we suggest that the flow of the glacier tongue is mainly controlled by the glacier geometry, while the presence of an ice-dammed lake and a supraglacial pond implies a hydrological influence as well. Taking the whole glacier and glacier tongue as two endmember avalanche sources, we assessed the potential runout distances of these two scenarios using the possible angle of reach and the Voellmy-Salm avalanche model. The assessments show that the avalanche of the whole glacier would easily travel a distance threatening the safety of the railway. In contrast, the detachment of the glacier tongue would threaten the railway only with a small angle of reach or when employing a low friction parameter in the Voellmy-Salm modeling.

1. Introduction

35 Glacier instabilities in the form of ice break-offs and avalanches are universal phenomena (Faillettaz et al., 2015; Haeberli et al., 2004; Jacquemart et al., 2020). Most of the glacier instabilities occur on steep glacier terminus or hanging glaciers, while recent studies show that ice detachment can also occur in low-angle (lower than around 20°) valley glaciers (Kääb et al., 2021a). The catastrophic detachment of part or even whole of a glacier can transport ice mass downstream to a distance of up to tens of kilometers, with a typical volume in the order of 10^6 m^3 . Due to the hazardous threats of glacier detachment to people's lives and infrastructure, distinguishing the detachment-prone glaciers from the non-threatening ones is crucial for hazard mitigation.

40 Several extraordinary low-angle glacier detachment events have been reported in recent years. One of the earliest events that was documented in detail was the destructive 2002 Kolka glacier detachment in Russia, which killed about 140 people due to the mass flow (Haeberli et al., 2004; Huggel et al., 2005). Another destructive event raising great attention was the 2016 detachments of two valley glaciers in the Aru mountain range in the western Qinghai-Tibet Plateau (QTP), which caused nine casualties (Bai and He, 2020; Gilbert et al., 2018; Kääb et al., 2018; Tian et al., 2016). In addition to these two well-known

45 events, a few historical detachments of valley glaciers are recently recognized and analyzed, such as the 2007 detachment of Leñas glacier in the Argentinian Andes (Falaschi et al., 2019), the three repeat detachments (in 2004, 2007, and 2016) of a glacier in the Amney Machen mountain range of the eastern QTP (Paul, 2019), and the two (2013 and 2015) detachments of the Flat Creek glacier in Alaska (Jacquemart et al., 2020). Recent research suggests that glacier detachments occur more frequently than previously thought (Kääb et al., 2021a).

50 A wide range of triggers can lead to a glacier detachment. Possible triggering factors include changes in ice thermal regime, morphology of a glacier, and atmospheric conditions (Gilbert et al., 2018; Tian et al., 2016, Kääb et al., 2021a). Some detachments occurred on surge-type glaciers. For example, the Kolka glacier and the Amney Machen glacier have experienced repeated surging in history (Kotlyakov, 2004; Paul, 2019). The detachments of several glaciers such as the Aru and Flat Creek glaciers were also preceded by geometric changes in the form of surge-like behaviors, although they were not known as surging

55 before (Gilbert et al., 2018; Jacquemart et al., 2020). Meanwhile, studies have highlighted that sudden detachments can occur on glaciers with no historical records of instability (Kääb et al., 2018; 2020).

The detachment of Aru glacier on the QTP has raised concerns on the stability of glaciers there, especially under intense climate warming. In past decades, air temperatures recorded by weather stations on the QTP have been increasing at a mean rate of $0.3\sim 0.4 \text{ }^\circ\text{C}\cdot 10\text{a}^{-1}$, which is twice the mean global rate (Chen et al., 2015). Considering that large-volume ice detachments can

60 occur on low-angle mountain glaciers, it is essential to investigate the long-term dynamics of glaciers prone to detachments and further assess their potential impacts. While previous studies of glacier ice valances and surge movements on the QTP mainly focused on the Karakorum and West Kunlun mountain regions where a large number of surge-type glaciers exist (Bhambri et al., 2020; Leinss et al., 2019; Yasuda and Furuya, 2015), little is known about glacier instabilities in the inner region of the plateau.

65 In this study, we present a comprehensive analysis of the dynamics of a small low-angle valley glacier (94.145°E, 37.678°N)
in the East Kunlun Mountains of QTP (Fig. 1). We refer to the glacier's name as 'KLP-37' since it is located at the Kunlun
Pass (KLP) of the East Kunlun Mountains and numbered 532EB037 in China's second glacier inventory (Guo et al., 2015).
We identified the glacier, which is close to the Qinghai Tibet railway and highway, during a field trip in the KLP region in
70 ice avalanche might be imminent.

To assess the stability of the KLP-37 glacier, we employed multi-sensor satellite imagery to characterize its morphological
changes and dynamics in the past 40 years. The changes in the terminus position of the glacier were tracked by interpreting
optical images from the Planet constellation and Google Earth. We used/generated six DEMs over the glacier between 1975
and 2018 to quantify the surface elevation variations. The 1975 DEM was reconstructed using a stereo image pair from the
75 Hexagon KH-9 reconnaissance satellite. Surface flow velocities of the glacier tongue from 2009 to 2020 were also mapped
using image cross-correlation. Combining the decadal geomorphic changes and surface velocities, we discuss the possible
mechanisms accounting for the dynamics of the KLP-37 glacier and estimate the potential runout distance if a failure of the
glacier tongue occurred in the future. We also discuss how the site-specific study on the KLP-37 glacier could provide new
insights into the glacier detachment hazard monitoring and assessment.

80 **2. Study site and remote sensing data**

2.1 Study site

The KLP is located in the central part of the East Kunlun Mountains in the inner QTP (Fig. 1a). The geomorphic pattern in the
KLP region was influenced by tectonic movement 1.1–0.6 Ma BP. During the maximum Quaternary glaciation (i.e., Wangkun
Glaciation) 0.7–0.5 Ma in the region, the areas of the glaciers were 3–5 times larger than those of the present glaciers (Wu et
85 al., 2001). The KLP-37 glacier rests on the northern slope of the East Kunlun Mountains. The lithology on the slope where the
glacier lies mainly consists of Triassic metamorphic sandstone and sand slate, with typical grain diameters of 2–5 cm (Wu et
al., 1982). The rock fragments are strongly weathered and filled with fine-grained (pelitic to sandy) sediments (Wu et al., 1982),
suggesting the KLP-37 glacier likely rests on a soft bed.

The KLP region nowadays is also tectonically active. The Kunlun fault, one of the principal left-lateral strike-slip fault systems
90 in the northern part of the QTP, runs for about 1600 km along the west-east and splays into two sub-fault segments at the KLP
(Fig. 1a). The Kunlun fault system generated a few $M_w > 7$ earthquakes in the last 100 years, including the most recent two in
2001 ($M_w 7.8$) and 1963 ($M_w 7.1$) (Lasserre et al., 2005). Notably, the 2001 event, with its epicenter only ~45 km west of the
KLP-37 glacier (Fig. 1a), induced several ice avalanche events (see the yellow dots in Fig. 1a) over the glaciers in the KLP
region (Jerome et al., 2004).

95 The KLP-37 glacier terminates about 3.3 km from the Qinghai-Tibet railway, which crosses the Xidatan basin along the west-

east direction (Fig. 1b). The Xidatan basin is also the northern permafrost boundary of the QTP (Wu et al., 2005). The climate is typically cold and arid: the annual mean air temperature is $-2.9\text{ }^{\circ}\text{C}$, and the average annual precipitation is about 400 mm, with most of the precipitation concentrating in summer from May to September (Luo et al., 2018). The snow line in this region is about 5100 m on the north slope and 5300 m on the south (Wu et al., 2001).

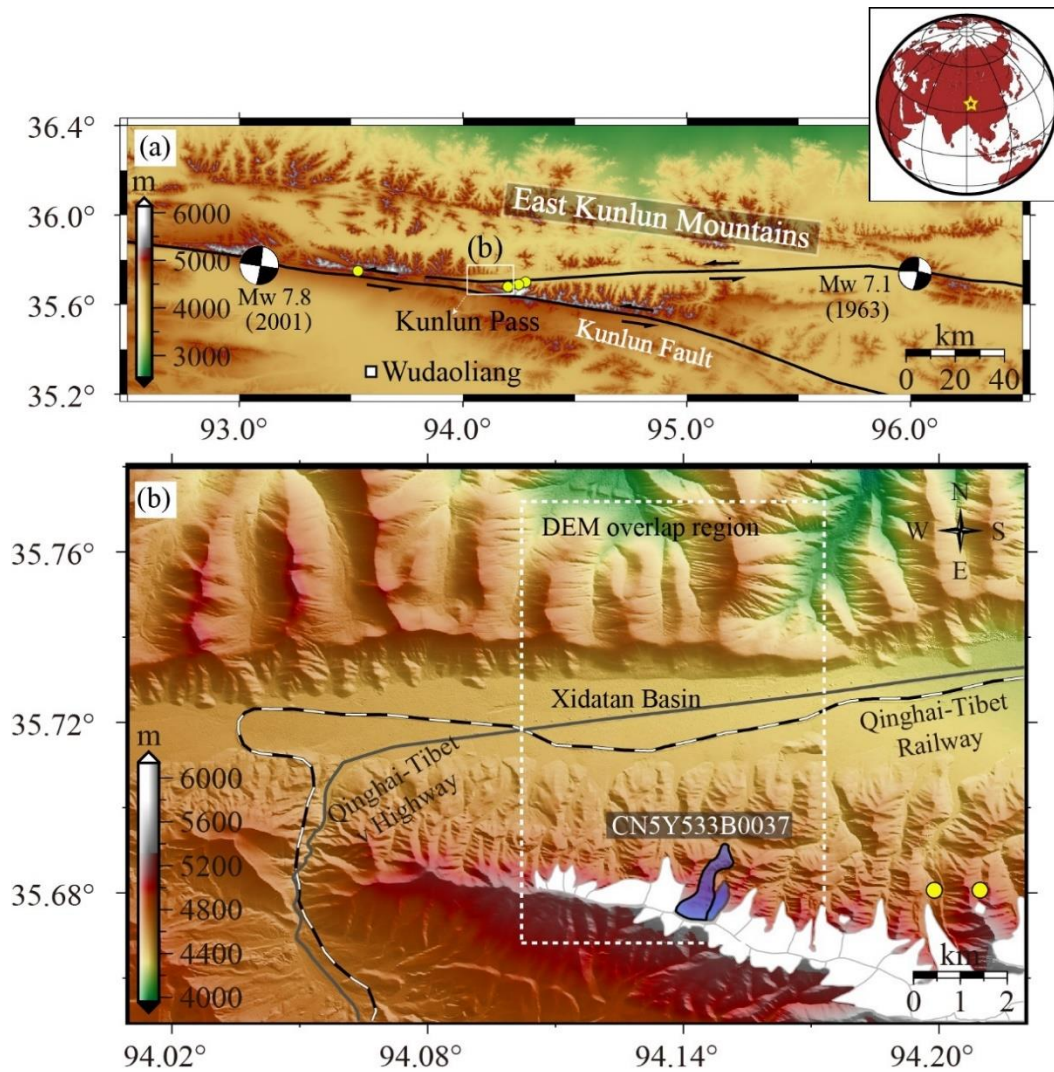
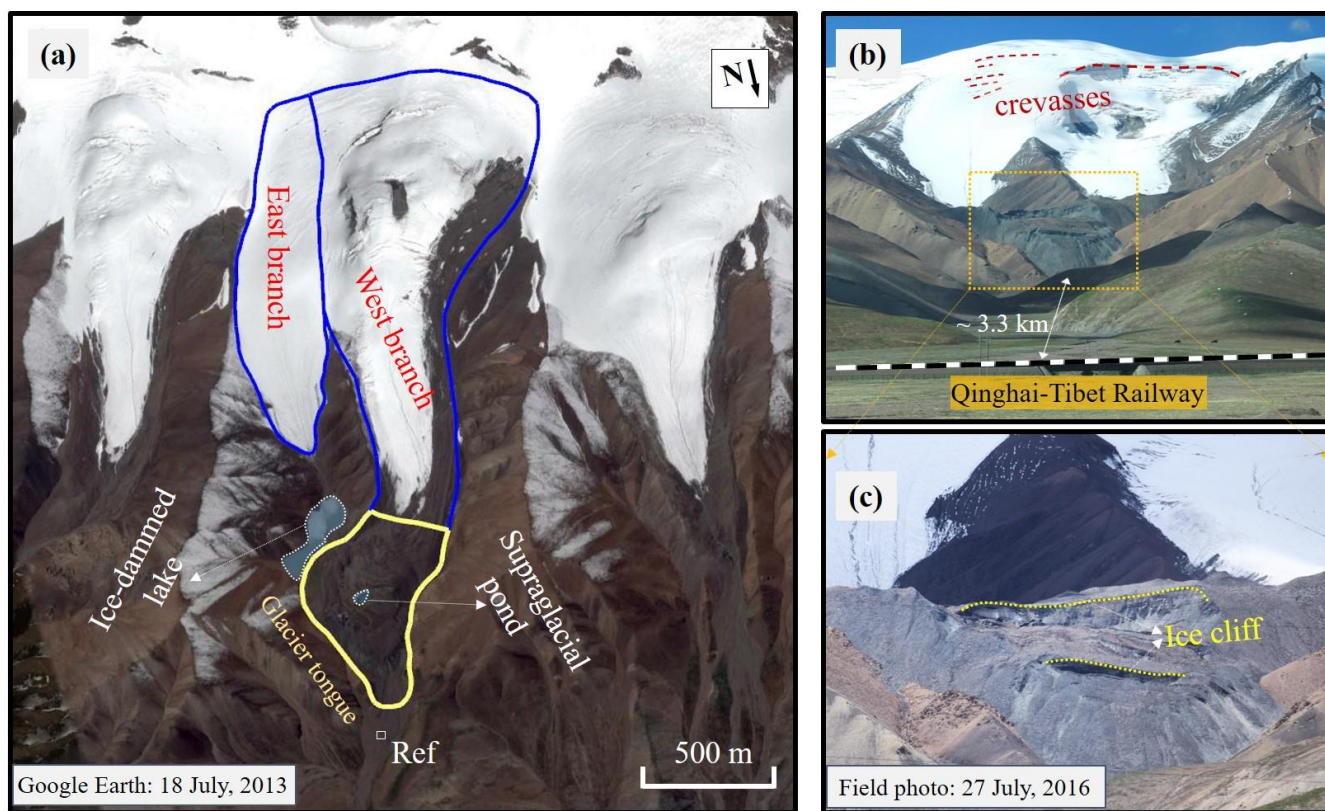


Figure 1: (a) The geological overview of the study area. The black lines depict the Kunlun fault traces. The yellow dots mark the ice avalanche locations induced by the 2001 Mw 7.8 earthquake (Jerome et al., 2004). The white square indicates the Wudaoliang Meteorological station. (b) The topography of the Kunlun Pass region. The white rectangle shows the overlap region of the DEMs used in this study. The polygons are the glaciers from the GAMDAM glacier inventory (Sakai et al., 2019), while the one filled with purple color is the KLP-37 glacier, whose west branch is outlined in thick black.

110

The KLP-37 glacier is a small low-angle valley glacier consisting of two branches (the GAMDAM glacier inventory, Sakai, 2019). Here our analyses mainly focus on the west branch, which has a length of about 2.06 km and a mean slope of about 20° . The elevation range of the glacier spans between 4650 and 5450 m. Compared to the east branch of the glacier, the west branch's terminus lies about 220 m lower (Fig. 2a). The width of the glacier gradually narrows from the accumulation zone to the downstream. From the satellite image taken in the summer of 2013 (Fig. 2a), we can observe an ice-dammed glacier lake in front of the glacier's east branch and a supraglacial pond on the west branch's tongue surface. The field photo on 27 June 2016 exhibits multiple horizontally distributed fissures at the glacier accumulation area (Fig. 2b). The developed crevasses, exposed ice cliffs, and glacier ice are also clearly visible in the tongue region, indicating the tongue is highly active (Fig. 2c).



115

Figure 2: (a) The outlines of the KLP-37 glacier (blue line) and tongue (yellow line) overlaid on a Google Earth image of 18 July 2013 (© Google Earth™). The ice-dammed glacier lake and a supraglacial pond are also shown. (b) and (c) are the field photos acquired by the author on 27 July 2016, which exhibit the crevasses and ice cliffs on the glacier surface. The rectangle annotated with “Ref” in (a) indicates the area for estimating image cross-correlation error (see Section 3.3).

120

2.2 Remote sensing data

Table 1 lists the satellite remote sensing data used in this study. The data types include optical orthoimages, stereo images, and multiple DEMs derived from both stereo-photogrammetry and SAR interferometry. All the data were referenced to the coordinate system of UTM zone 46 N.

125 **Table 1. Satellite imagery and DEMs used in this study.**

Data	Date	Spatial Resolution (m)	Data type	Purpose
RapidEye	2009/08/30; 2010/09/07; 2012/09/12; 2013/08/04; 2015/10/12;	5	Orthoimages	Geomorphic change
PlanetScope	2016/09/10; 2017/08/09; 2018/07/24; 2019/08/06; 2020/08/29; 2021/03/23;	3	Orthoimages	Terminus advance Flow velocity
Google Earth	2013/08/15	~ 1	-	Geomorphic change
KH-9	1975/12/10	7.6	Stereo images	Terminus advance Elevation change
ASTER	2018/01/12	15	Stereo images	Elevation change
SRTM-X/C	2002/02	30	DEM	Elevation change
HMA DEM	2010/12/05; 2014/08/27	8	DEM	Elevation change
TanDEM-X	2011–2014	12	DEM	GCP elevation Elevation reference

130 Glaciers changes are often mapped on the freely available Landsat and ASTER satellite images, which commonly have a resolution of 10–30 m (Bolch et al., 2011; Scherler et al., 2011). Considering that KLP-37 is a small valley glacier with a width of only about 200 meters, we used five RapidEye (5 m spatial resolution) and six PlanetScope (3 m) orthoimages acquired by Planet’s constellation of CubeSats between 2009 and 2021. All the Planet scenes are ortho products and consist of visible and near-infrared frames. We also used the high-resolution Google Earth image to assist in the boundary delineation and detailed morphology characterization.

135 We used a stereo-pair acquired by the Hexagon KH-9 spy satellite to reconstruct the topography of KLP-37 in 1975. The KH-9 images (image IDs: DZB1211-500024L002001 and DZB1211-500024L003001), with a ground resolution of about 7.6 m, were scanned by the U.S. Geological Survey (USGS) at a resolution of 7 micrometers. The formation procedure of the KH-9 DEM using stereo-photogrammetry will be detailed in Section 3.2.1. We also generated the orthorectified KH-9 images, from which the glacier boundary was further identified.

In addition to the KH-9 DEM, we used another five DEMs in different periods between 2000 and 2018 to infer the elevation changes of the KLP-37 glacier after 1975 (see Table 1). Of the five DEMs, three were obtained from optical stereo-image photogrammetry, and the other two were generated using SAR interferometry. The SRTM and HMA DEMs are publicly

140 available, and the commercial TanDEM is provided by the German Aerospace Center. The latest ASTER DEM (2018) was
generated from an ASTER stereo-image pair acquired by the Terra satellite (Hirano et al., 2003). Two 8-meter High Mountain
Asia (HMA) DEMs (2010 and 2014) were generated from very-high-resolution imagery from Worldview-1/2 satellites by
Shean (2017). The SAR interferometry derived DEMs include the SRTM (2000) and TanDEM, with spatial resolutions of 30
145 from radar data with different wavelengths (i.e., C-band and X-band). Here both the C- and X-band SRTM DEMs were used
to correct for the penetration depth of radar wavelength. The commercial TanDEM was produced from the TerrSAR-
X/TanDEM-X SAR images acquired between January 2011 and September 2014, representing an average estimate over the
period. We, therefore, did not use the TanDEM to calculate elevation changes of the glacier surface. Instead, the TanDEM was
taken as a reference to evaluate the accuracy of the other DEMs because of its relatively high vertical accuracy (~2 m) (Riegler
150 et al., 2015). The TanDEM was also used to extract the elevations of the selected ground control points (GCPs) when
constructing DEM with the ASTER stereo-images (see Section 3.2.1).

3. Methodology

3.1 Derivation of glacier terminus changes

We manually digitized the boundary of the glacier from the orthorectified KH-9 image and the 11 Planet orthoimages. The
155 boundaries of the snow-covered part of the KLP-37 glacier were cross-checked against the GAMDAM glacier inventory (Sakai,
2019). We identified the center point of the glacier terminus in each image and then estimated the advance distance between
two consecutive periods. To avoid the influence of spatial resolution on the determination of the terminus center point, all the
images were resampled into a common geometry with a spatial resolution of 3 m, the same as the resolution of the PlanetScope
images. By dividing the advance distance by each image pair's time span, we further estimated the terminus advance velocities
160 (v_t) during 1975 and 2019. The uncertainty of the velocity estimate can be written as (Hall et al., 2003; Rashid et al., 2020)

$$\varepsilon_{v_t} = (\sqrt{r_1^2 + r_2^2} + \varepsilon_{geo})/\Delta t \quad (1)$$

where r_1 and r_2 are spatial resolutions of the two images, respectively; ε_{geo} is the relative georeferencing error between
the two images; Δt is the time span of the two images. Note that we estimated ε_{geo} for the Planet image pairs from off-
glacier cross-correlations, and for the KH-9–Planet image pair from coordinate differences at the selected ground control points.

165 3.2 Surface elevation changes from DEM differencing

3.2.1 DEM extraction from stereo images

We used the HEXIMAP toolbox, developed by Maurer et al. (2016) and coded in MATLAB with an automated pipeline, to
generate DEMs from the KH-9 stereo images. HEXIMAP combines computer-vision concepts with traditional
photogrammetric methods to achieve a satisfactory solution of DEM accuracy. The OpenCV library is used in HEXIMAP for

170 surface feature matching, uncalibrated stereo rectification, and semiglobal block matching. Each digital KH-9 image provided
by the USGS consists of two sub-frames with some overlap. The preprocessing steps thus include the stitching of sub-frames
and cropping to the region of interest. Because the exterior parameters of KH-9 images are unavailable, HEXIMAP first
generates a DEM with only rough geographical coordinates and then refines the DEM by matching it to an external reference
DEM (Maurer et al., 2016). Here we used the TanDEM as the reference DEM and finally extracted the KH-9 DEM with a
175 spatial resolution of 15 m. Fig. S1 (see the Supplementary file) shows the generated KH-9 DEM for the study area.

We used the open-source ASP (Ames Stereo Pipeline, v2.6.2) software developed by NASA to extract DEMs based on the
ASTER stereo images. The ASP software provides a program called “aster2asp”, which implements a straightforward pipeline
for processing ASTER stereo images and extracting DEM (Shean et al., 2016). To ensure the DEM accuracy, we selected 12
GCPs on the high-resolution Planet image (2016/10/10) and determined the elevations of GCPs with the TanDEM data. The
180 ASTER DEM was also generated with a spatial resolution of 15 m.

3.2.2 DEM co-registration and differencing

With the KH-9 (1975), SRTM (2000), HMA (2010 and 2014), and ASTER (2018) DEMs, we formed four pairs with
consecutive times to perform DEM differencing. All the DEMs were resampled into the overlap region shown in Fig. 1b (see
the white box) to a spatial posting of 15 m. The DEM pairs need to be co-registered to minimize the errors associated with
185 geometric shifts. We used the method that relies on the geometric relationship between the shift vectors and the slope and
terrain aspect to coregister the DEM pairs (Nuth and Kääb, 2011). The glacierized regions and the area with a slope smaller
than 10° were excluded before the coregistration. Fig. S2 shows an example of DEM differences before and after the co-
registration with the two HMA DEMs (see Table 1), demonstrating a remarkable reduction of residuals due to geometric shifts
between DEMs. After the co-registration, the older DEM of a pair was then resampled using the cubic interpolation method
190 with a resampling posting of 15 m. Elevation differences were calculated by subtracting the older DEM from the younger
DEM such that glacier thickening values are positive. We also calculated volume changes over the glacier tongue area (the
yellow polygon in Fig. 2a) during different periods based on the elevation change estimates.

Two possible systematic biases resulted from (1) the penetration of radar waves and (2) the seasonal snow cover on the glacier
should be corrected in DEM differencing. We used the SRTM-C DEM to calculate elevation changes between 1975/12/12–
195 2000/02 and 2000/02–2010/12/05. Considering the low penetration depth of X-band radar into snow/ice surface, we used the
X-band SRTM DEM (SRTM-X) as a reference to correct for the bias of the SRTM-C DEM. The elevation differences over the
KLP-37 glacier between the X- and C-band SRTM DEMs were calculated, from which we found that the elevation difference
was generally positively proportional to surface elevation (Fig. S3). The mean elevation differences were about 0.43 m and
2.36 m for regions below and above 5000 m, respectively. The small penetration depth in the glacier tongue region is probably
200 due to the debris cover on the surface. Following previous studies (e.g., Li et al., 2021), we implemented a linear fitting to the
elevation differences and then applied the penetration correction with the fitted model (i.e., $y = 0.046h - 21.5335$). Snow

cover changes due to the different acquisition times of DEMs may also contribute to the estimate of glacier elevation change (Gardelle et al., 2013). This effect is usually referred to as the seasonality artifacts in DEM differencing. All the DEMs we used were acquired during winter except for the HMA DEM of late August in 2014. We did not apply adjustments to winter-winter DEM pairs because KLP-37 is a summer-accumulation type glacier. However, elevation changes for the summer-winter DEM pairs (i.e., HMA10-HMA14 and HMA14-ASTER) need to be corrected by considering four to five months of time differences. Similar to previous studies (Li et al., 2017), we conservatively adjusted the HMA DEM in 2014 by applying an empirical bias correction of 0.1 m per month due to the scarcity of snow depth documentation around the glacier.

3.2.3 Uncertainty assessment

Elevation change uncertainty estimates were calculated based on off-glacier elevation changes in the DEMs' overlap region (see the white rectangle in Fig. 1b). We calculated the uncertainty statistically by dividing the altitude into different bands with a 50 m interval. We assumed that the error for each pixel of elevation change ($\varepsilon_{\Delta h}^i$) is equal to the standard deviation of each elevation band, which can be calculated according to standard principles of error propagation (Gardelle et al., 2013)

$$\varepsilon_{\Delta h}^i = \frac{\sigma_{\Delta h}^i}{\sqrt{N_{\text{eff}}}}, \quad (2)$$

where $\sigma_{\Delta h}^i$ is the standard deviation of the elevation changes in the i_{th} elevation band; N_{eff} represents the number of independent values in the band, which can be calculated as

$$N_{\text{eff}} = \frac{N_{\text{tot}} P_s}{2 \cdot d}, \quad (3)$$

where P_s is the pixel posting of the DEM; N_{tot} is the total number of elevation change measurements in the elevation band; d is the distance of spatial autocorrelation of the elevation change maps, which can be obtained by a least-square fit to the experimental, isotropic variogram of all off-glacier elevation differences (Wang and Käab, 2015; Magnússon et al., 2016). The autocorrelation distances for the four DEM pairs were 286 m (KH-9-SRTM), 167 m (SRTM-HMA10), 189 m (HMA10-HMA14), and 909 m (HMA14-ASTER), respectively, with a mean value of about 388 m, similar to the typical value of about 500 m by previous studies (McNabb et al., 2019). The error of the glacier volume change ($\varepsilon_{\Delta V}$) was derived from the uncertainty of elevation change:

$$\varepsilon_{\Delta V} = \sqrt{\sum (A_i \cdot \sigma_{\Delta h}^i)^2}, \quad (4)$$

where A_i is the area of each elevation band.

3.3 Surface velocity from image cross-correlation

To investigate the dynamics of the KLP-37 glacier tongue, we applied cross-correlation to the orthorectified Planet images to obtain two-dimensional surface displacements. The acquisition 2015/10/12 and 2021/03/23 were not used because the glacier

230 tongue was partially affected by snow cover. Seven consecutive image pairs were formed and correlated for obtaining surface velocities during each period. We extracted the near-infrared band of the Planet images, i.e., the sub-band that has the longest wavelength, to implement the correlation measurement. This is because the long-wavelength band is generally less affected by cloud and has a higher radiometric magnitude.

235 The freely available, open-source Micmac software was used to implement the sub-pixel image cross-correction (Rosu et al., 2015; Rupnik et al., 2017). The correlator program “MM2DPosSism” provided in Micmac employs a hierarchical matching scheme using normalized cross-correlation (NCC) with a non-linear cost function to find the most likely match for each pixel. The matching cost function is evaluated from the NCC coefficient considering only correlation coefficients $C \geq C_{\min}$. Micmac also adopts a unique regularization parameter r to smooth displacement field and reduce noise and outliers, which allows the use of smaller matching template windows targeting small landscape features. Here we set values of 0.5 and 0.3 for C_{\min} and r , respectively, and a moving window of 9×9 pixels in the correlation processing. In addition, we specified the main flow direction (i.e, $NE15^\circ$) as the privileged direction of regularization. The flow velocity’s uncertainties primarily result from the imprecise matching of the surface features on the glacier. Similar to previous studies (Rupnik et al., 2017), we inferred the uncertainty of flow velocity using the correlation estimate at a stable and plain surface below the glacier terminus (see the white rectangle in Fig. 2a).

245 **3.4 Avalanche Runout Hazard Assessment**

We estimated the maximum runout distance to quantitatively assess the possible influence of the glacier detachment. We first empirically estimated the maximum runout distance using the angle of reach (also called “Fahrböschung”), which is defined as $\arctan(H/L)$, whereas L is horizontal reach of avalanche mass and H is elevation drop. Note H is measured from the avalanche start point to the stop point. Previous investigations have shown that Fahrböschung value for low-angle glacier detachments typically ranges between 5° and 10° (Kääb et al., 2021a). Given the possible avalanche start and stop points, we can thus roughly estimate the maximum runout distance.

255 We also quantitatively estimated the extent of hazard-prone areas using avalanche-dynamics modeling. We employed the Voellmy-Salm (VS) model to simulate the possible runout extent and flow height of ice materials. The VS model was originally developed to investigate the detailed flow patterns and dynamics related to pure snow avalanches (Bartelt et al., 1999); while the model has also been widely used to simulate the runout distance of glacier/ice avalanche events (Allen et al., 2009; Bai and He, 2020; Evans et al., 2009). The VS model divides avalanche flow resistance into a speed-independent Coulomb-type friction (friction coefficient μ) and a velocity-dependent, turbulent friction (friction coefficient ξ , units: $m \cdot s^{-2}$) (Bartelt et al., 1999). Here, we empirically determined the ranges of μ and ξ from previous studies because it is impossible to obtain these friction parameters directly. Retrospective analyses of glacier/ice avalanche events from different glacial environments based on the VS model have shown that the best-fit frictional values generally range between 0.05 and 0.2 for μ , and between 1000 and

4000 m·s⁻² for ξ (Allen et al., 2009). Studies of a few glacier detachment events also have revealed friction parameters laying within the above ranges. For instance, the best-fit μ for the first and second Aru glacier detachments are 0.11 and 0.14, respectively (Kääb et al., 2018); the 2002 Kolka detachment has best-fit values of 0.05 and 2700 m·s⁻² for μ and ξ , respectively (Allen et al. 2009).

265 We used the open-source software MASSFLOW to implement the modeling (Ouyang et al., 2013). MASSFLOW contains the VS model and allows for the simulation of rapid mass movements accounting for momentum and including processes of friction, fluidization, and erosion. The input datasets of the VS model consist of a DEM for generating a meshed grid and a source file containing the geographical extent and thickness of the avalanche materials. Here we used the 7-meter HMA DEM acquired in 2014 as the input topography. The ice thickness was derived from Farinotti et al. (2019), who provided an ensemble-
270 based estimate for the ice thickness distribution of all glaciers included in the Randolph Glacier Inventory (RGI) apart from the Greenland and Antarctic ice sheets. However, the ice thickness for KLP-37 does not include the tongue region. Given that the ice thickness in KLP-37 shows a homogenous pattern, with 86% of pixels having a thickness ranging between 25 and 45 m, we took the mean value of the known pixels (i.e., 32±6 m) as the glacier tongue ice thickness.

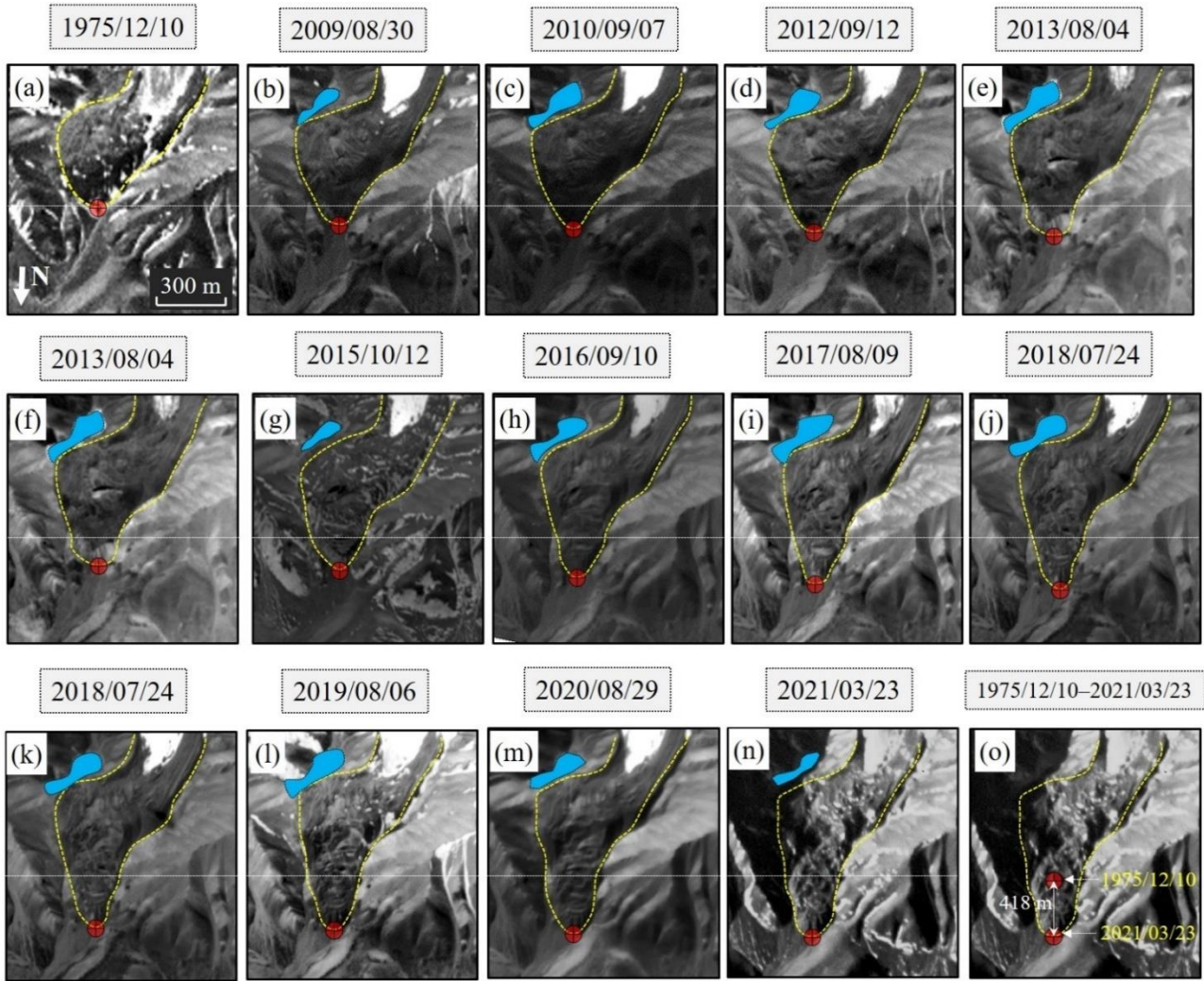
4. Results

275 4.1 Morphological changes and terminus advance

The optical KH-9 and Planet satellite images enable us to inspect the morphological changes of the KLP-37 glacier in the past 46 years. A time-lapse of the optical images covering the full glacier are shown in Fig. S4, and the zooms of the glacier tongue region for a clear inspection are shown in Fig. 3. Satellite images show that the transverse crevasses in the glacier cirque had commenced in 1975 and became more evident in the following years (see the red arrows in Fig. S4). Specifically, the crevasses' length and width changed apparently after 2013. The highly developed crevasses in the glacier accumulation region since the
280 1970s and the widening of the crevasses in recent years indicate that the glacier may develop towards destabilization. Also, the glacier tongue exhibits a swollen body with a steep front in the KH-9 image (Fig. 3a), indicating a large amount of ice mass had been deposited there by 1975.

Satellite optical images also clearly show the evolution of the ice-dammed lake (the light blue polygons in Fig. 3) developing in the front of the glacier's west branch. The lake was not visible in the 1975 image. However, we cannot rule out the possibility that the coarse resolution (~ 7.6 m) of the KH-9 image may hinder the identification of the lake. The high-resolution Google Earth image in 2005 shows that the ice-dammed lake had appeared before then (Fig. S5). To investigate the changes in lake area over time, we delineated the boundary of the lake based on the Planet and Google Earth images and estimated the lake area between 2005 and 2019 (see Table S1). The uncertainty in delineating the lake was obtained from five independent digitizations (Paul et al., 2017). The lake area peaked in summer and decreased in winter. The lake area showed an expansion
285 trend in recent years, with the smallest value (3745±229 m²) in the winter of 2010 and the largest value (21276±1646 m²) in
290

the summer of 2017. A small supraglacial pond developed in the depressions on the glacier tongue surface; The pond (Figs. 2a and 3) appeared in 2013 and disappeared in 2017.



295 **Figure 3: Optical satellite images covering the KLP-37 glacier tongue. (a) Hexagon KH-9 image acquired on 1975/12/10**
 (© U.S. Geological Survey); (b-n) Planet images acquired between 2009/09/07 and 2021/03/23 (© Planet Labs); (o)
 Comparison of the glacier terminus position between 1975 and 2021. The horizontal white dotted lines provide a
 reference for the terminus position in 1975. The blue polygons represent the ice-dammed glacier lake.

300 The glacier terminus showed a stepwise advance pattern (see the red points at the glacier snout in Fig. 3) between 1975 and
 2021. Table S2 lists the terminus point coordinates in each satellite image, and Fig. 4 shows the changes in terminus advance
 velocities during periods between the consecutive image acquisitions. The glacier tongue moved downstream and narrowed
 due to the topographic blocking on both sides. The glacier terminus' total advance distance was about 418 ± 24.13 m in the past

46 years (Fig. 3o). The advance velocity between 1975 and 2009 was about $4.55\pm 0.46 \text{ m}\cdot\text{a}^{-1}$, and the velocity rose to more than $10 \text{ m}\cdot\text{a}^{-1}$ after 2009. The velocities were stable within each period of 2009–2015 and 2015–2021 but jumped between 2015 and 2016. The mean velocity was $15.70\pm 3.02 \text{ m}\cdot\text{a}^{-1}$ during 2009–2015 and $30.88\pm 2.36 \text{ m}\cdot\text{a}^{-1}$ during 2015–2021.

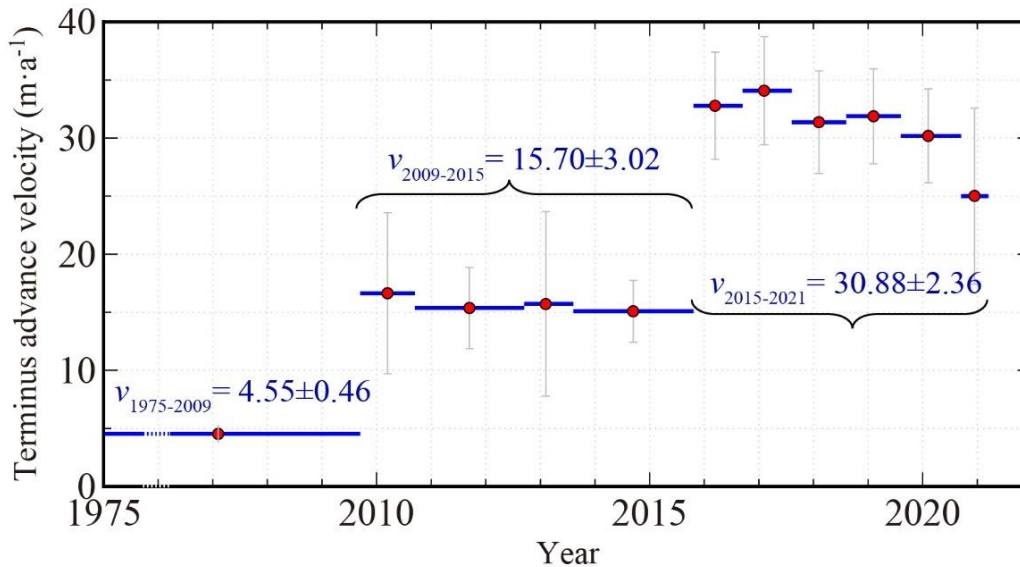


Figure 4: Terminus advance velocities and the associated uncertainties (the light gray error bars) of the KLP-37 glacier estimated from KH-9 and Planet images. We also annotated the mean velocities during three periods: 1975–2009, 2009–2015, and 2015–2021. Note that the time axis during 1975–2009 is not equally posted for a better presentation.

310 4.2 Surface elevation and volume changes

We evaluated the accuracies of the DEMs before DEM differencing using the TanDEM as a reference. Most of the elevation differences range between -10 and 10 m (see Fig. S6). The mean values of the off-glacier elevation differences between the TanDEM and other DEMs are all smaller than 0.2 m, indicating that the accuracies of the DEMs we used are feasible for inferring the elevation changes of the KLP-37 glacier by DEM differencing.

315 Surface elevation changes of the KLP-37 glacier from DEM differencing overall exhibit thinning in the glacier source region and thickening in the glacier tongue (Figs. 5a-d). The void regions mainly appear in the accumulation area of the glacier's west branch, where the slopes are steep and intense crevasses developed. We selected a specific point 'T' with a window size of 3×3 pixels ($\sim 2000 \text{ m}^2$) in the center of the accumulation region (see Fig. 5a) and found that the elevation differences at this point for the KH-9–SRTM, SRTM–HMA10, HMA10–HMA14, and HMA14–ASTER pairs are -1.64 ± 0.77 , -0.22 ± 0.15 , -0.90 ± 0.31 , and $-0.02\pm 0.34 \text{ m}\cdot\text{a}^{-1}$, respectively. Although the estimate from the HMA14-ASTER DEM pair had considerable
 320 uncertainty, the elevation change rate at point 'T' showed a decreasing trend during 1975–2018. Note the estimates for the

KH-9-SRTM and SRTM-HMA10 DEM pairs were influenced by radar penetration depths. To infer how much the radar penetration depths would impact the elevation change estimates, we calculated the elevation differences between the X-band and C-band SRTM and obtained an elevation difference of 2.44 m at the point 'T'. Considering that we had applied a correction of 2.13 m (given the correction model of $y=0.0046 \times h - 21.5335$ and the elevation of 5145 m at the point 'T') to the SRTM DEM, a residual of 0.31 m would remain in the elevation change estimates. We thus inferred that the elevation change errors due to SRTM penetration were about $0.01 \text{ m} \cdot \text{a}^{-1}$ and $0.03 \text{ m} \cdot \text{a}^{-1}$ for the KH-9-SRTM and SRTM-HMA10 DEM pairs, respectively.

The east branch of KLP-37 did not show a retreat behavior in the past 40 years, while elevation differences there showed an overall thinning pattern. The mean elevation changes over the whole east branch were about -0.18 ± 0.12 , -0.32 ± 0.15 , -0.48 ± 0.09 , and $-0.82 \pm 0.55 \text{ m} \cdot \text{a}^{-1}$ for the four DEM pairs, respectively. The continued thinning of the glacier's east branch presumably explains the expansion of the ice-dammed glacier lake, which develops in the front of the east branch and receives the meltwater from the glacier directly.

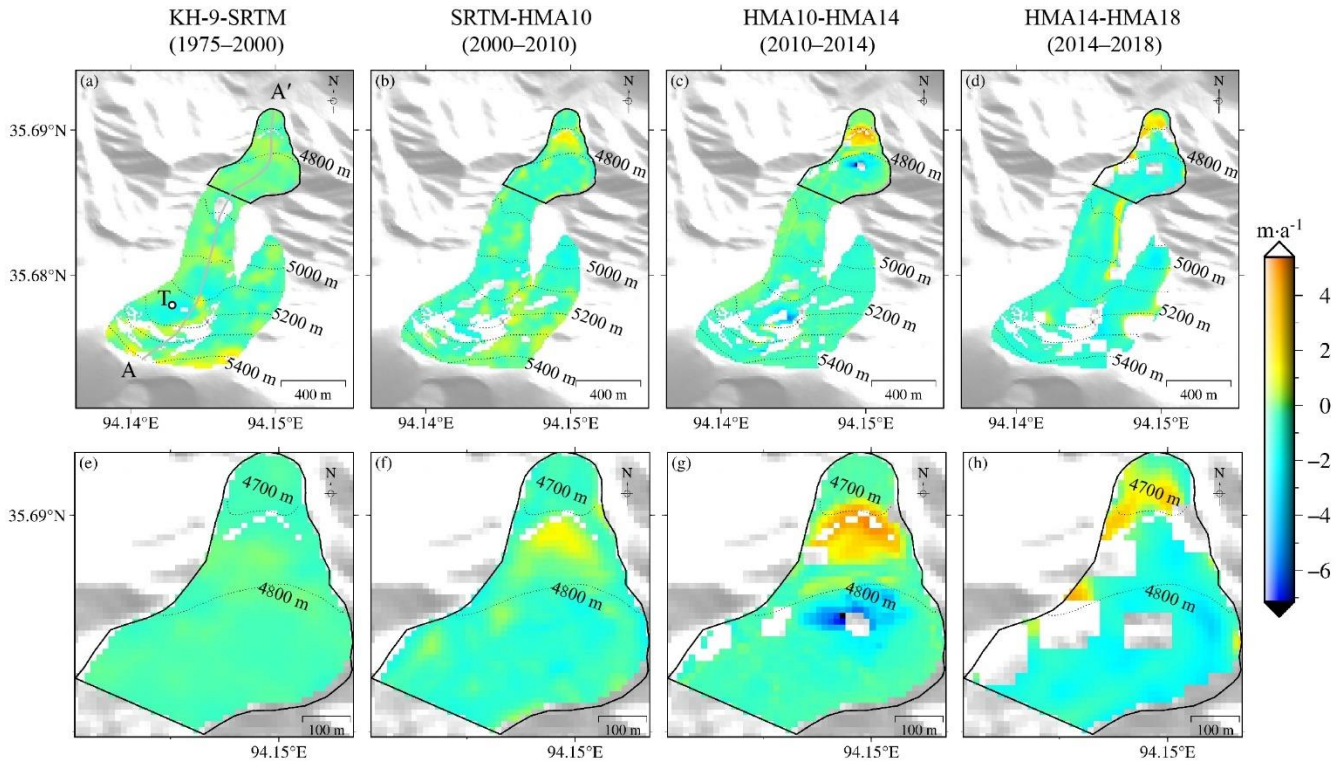


Figure 5: Surface elevation changes of KLP-37 glacier between 1975 and 2018. (a-d) Elevation changes over the full glacier for the DEM pair KH-9-SRTM (1975–2000), SRTM-HMA10 (2000–2010), HMA10-HMA14 (2010–2014), and HMA14-ASTER (2014–2018), respectively. (e-f) Amplified elevation changes over the glacier tongue region for the four DEM pairs. The black dotted lines indicate the elevation contours.

The elevation changes over the glacier tongue region are enlarged and shown in Figs. 5e-h. We can observe evident elevation increases in the front part of the tongue and widespread thinning just above the elevation thickening area. Specifically, thinning was prevalent between the 4750 m and 4880 m for the SRTM–HMA10 and HMA14–ASTER DEM pairs. The snout of the elevation thickening area continually advanced from 1975 to 2018, with a remarkable advance during 2014–2018. Elevation changes confirm the stepwise glacial terminus advance (see Section 4.1) and imply a slow surge-like mass transfer process in the tongue area. This kind of flow behavior resembles the surging movement of the surge-type glacier, which has also been reported on the Aru or Amney Machen glaciers preceding the occurrences of ice detachments (Kääb et al., 2021a; Paul, 2019). However, we cannot conclude that KLP-37 is a surge-type glacier because we did not capture periodical alternations between long periods of slow flow and short periods of fast flow. We calculated the volume changes over the glacier tongue and found that the volume decreases were higher than the increases for all the four DEM pairs (Table 2). The net volume changes calculated from the four DEM pairs were -1.54 ± 1.18 , -5.74 ± 1.47 , -0.49 ± 0.11 , and $-3.44 \pm 1.87 \times 10^5 \text{ m}^3$, respectively, with a total net volume change of $-11.21 \pm 2.66 \times 10^5 \text{ m}^3$, indicating the continued loss of mass over the glacier tongue region.

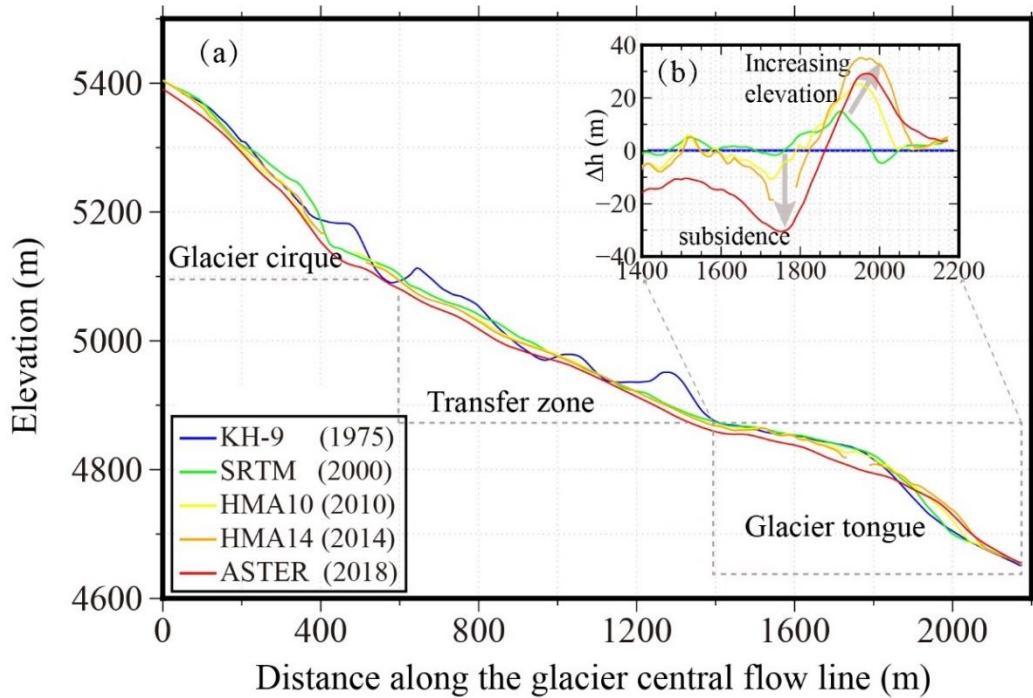


Figure 6: Glacier surface topography extracted from the five DEMs along the glacier central flow line AA' (Fig. 5a).

The inset shows the elevation changes along the profile with respect to the KH-9 DEM in 1975.

Fig. 6 shows the changes of surface topography from 1975 to 2018 along the glacier's central flow line (see AA' in Fig. 6a). We roughly divided the glacier into three parts: glacier cirque ($> 5100 \text{ m}$), transfer zone ($4880\text{--}5100 \text{ m}$), and the glacier tongue ($4700\text{--}4880 \text{ m}$). The cirque zone has a mean steep slope angle of about 34° , while the slope becomes gentle in the transfer

zone with a mean slope of 19°. Both the glacier cirque and transfer zone exhibited an overall subsidence pattern. The glacier tongue can be further divided into thinning and thickening parts at an elevation of about 4800 m. Notably, the thinning rate in the glacier tongue region was much higher than that in the transfer zone (see the subsidence arrow in Fig. 6b). The part above 4800 m continually subsided while the lower part showed increasing elevation, with the maximum of elevation changes moved toward the glacier terminus progressively (Fig. 6b).

Table 2. Net volume changes over the glacier tongue region calculated from the four DEM pairs.

DEM pairs	Time span (years)	Net volume change ($\times 10^5 \text{ m}^3$)
KH-9-SRTM	24.2	-1.54 \pm 1.18
SRTM-HMA10	10.8	-5.74 \pm 1.47
HMA10-HMA14	3.73	-0.49 \pm 0.11
HMA14-ASTER	3.38	-3.44 \pm 1.87

Uncertainties associated with the glacier surface elevation changes were evaluated with the statistics of off-glacier elevation differences based on Equation (2). The uncertainties of elevation changes generally increase with elevation (Fig. 7). The mean uncertainties of elevation changes over the glacier tongue region (4700–4880 m) were about 0.04, 0.08, 0.02, and 0.41 $\text{m}\cdot\text{a}^{-1}$ for the KH-9-SRTM, SRTM-HMA10, HMA10-HMA14, and HMA14-ASTER DEM pairs, respectively. Elevation changes in the DEM accumulation region ($>5100 \text{ m}$) had relatively higher uncertainties, with mean values of 0.06, 0.06, 0.03, and 0.54 $\text{m}\cdot\text{a}^{-1}$ for the four DEM pairs.

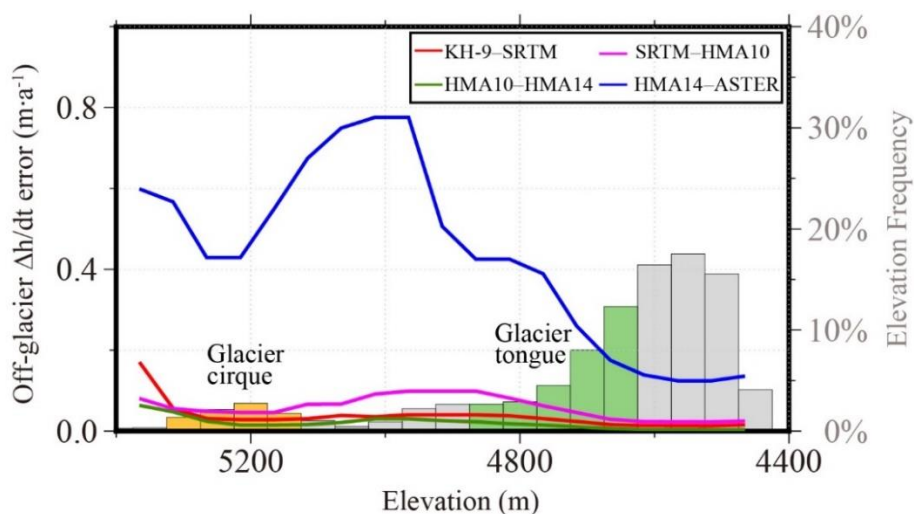


Figure 7: Uncertainty of elevation change estimate as a function of elevation bands (the lines) in the off-glacier region. The right axis annotates the frequency number of each elevation band. The elevation bands with yellow and green colors represent the glacier cirque and tongue ranges, respectively.

4.3 Surface flow velocities

Fig. 8 shows the surface flow velocities of the KLP-37 glacier tongue from the cross-correlation of seven Planet image pairs. We did not show the correlation result for the image pair 2013/08/04–2016/09/10 because 56% of the pixels within the tongue region have null values due to the low correlation coefficient, probably resulting from the remarkable change of surface features on the glacier. The mean uncertainty of flow velocity inferred from image correlations at the reference region (see Fig. 2a) was about 2.4 m. The velocity field exhibited an acceleration pattern during 2009/08/30–2020/08/29 (Fig. 8), which is consistent with the advance pattern of the glacier terminus (see Section 4.1). The flow of the glacier was distinguishable from the surrounding area for velocity field after 2016, especially at the glacier front region. The maximum flow velocity within the glacier tongue area reached about $30 \text{ m}\cdot\text{a}^{-1}$ after 2016, comparable to the estimated snout advance rate ($30.88\pm 4.45 \text{ m}\cdot\text{a}^{-1}$) between 2015 and 2021.

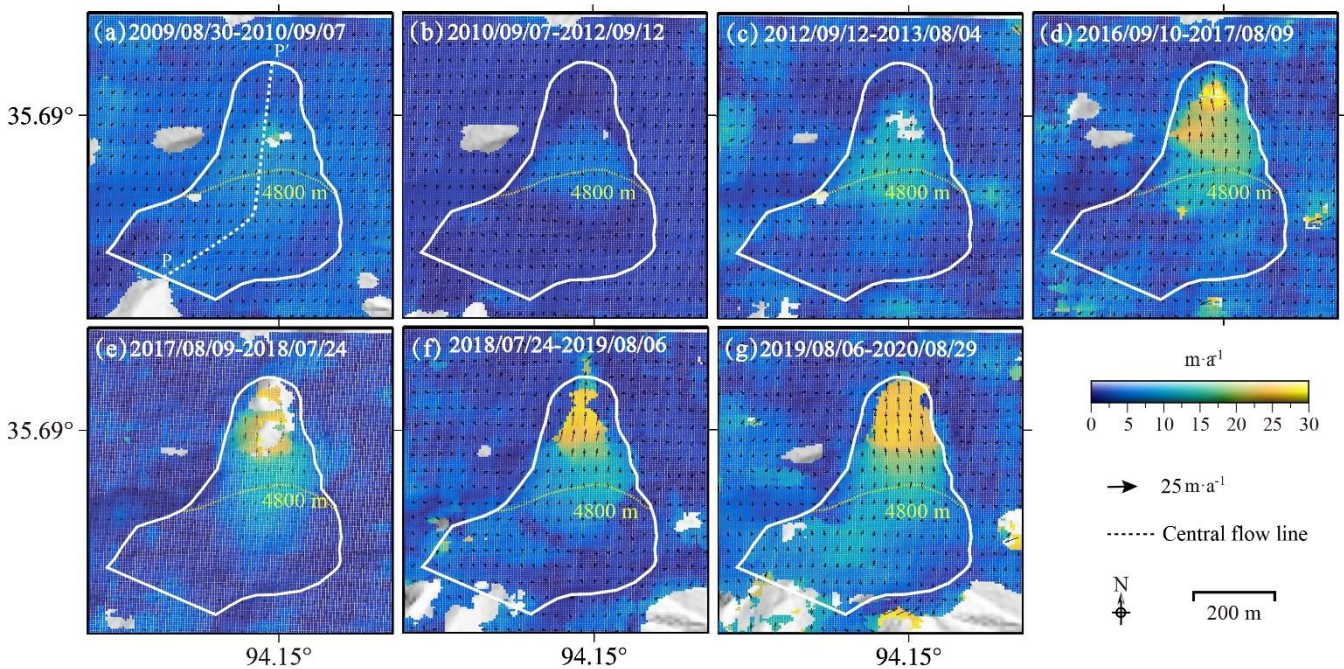


Figure 8: Surface velocities over the glacier tongue of KLP-37 from image cross-correlation based on the seven Planet image pairs. The profile PP' represents the central flow line, and the arrows mark the flow direction. Basemap: Courtesy of Google Earth™.

We found that the velocity field showed different spatio-temporal patterns below and above 4800 m, where the glacier flow direction changed. Peak velocity in each observation period was observed in the lower part of the glacier tongue. Evident flow acceleration occurred below 4800 m between 2013 and 2016. The maximum velocities within the glacier tongue (the white polygon in Fig. 8) were about $15.3\pm 2.1 \text{ m}\cdot\text{a}^{-1}$ (2012/09/12–2013/08/04) and $29.4\pm 3.2 \text{ m}\cdot\text{a}^{-1}$ (2017/08/09–2018/07/24) for the

390 periods before and after 2013, respectively. Note the maximum values were determined on a pixel-by-pixel basis. Fig. 9 shows
the velocity and topography variations along the central profile PP' (location shown in Fig. 8a). The velocities on the profile
were relatively stable above 4800 m before 2019 with a mean velocity of $4.6 \pm 1.5 \text{ m}\cdot\text{a}^{-1}$, while the mean value velocity doubled
($9.8 \pm 1.4 \text{ m}\cdot\text{a}^{-1}$) during 2019–2020. The mean velocities below 4800 m for the periods of 2009–2010 and 2019–2020 were
 6.3 ± 1.8 and $22.3 \pm 3.2 \text{ m}\cdot\text{a}^{-1}$, respectively. The more than tripled mean velocity below 4800 m in the past decade suggests that
395 the glacier tongue has been getting more active towards destabilization.

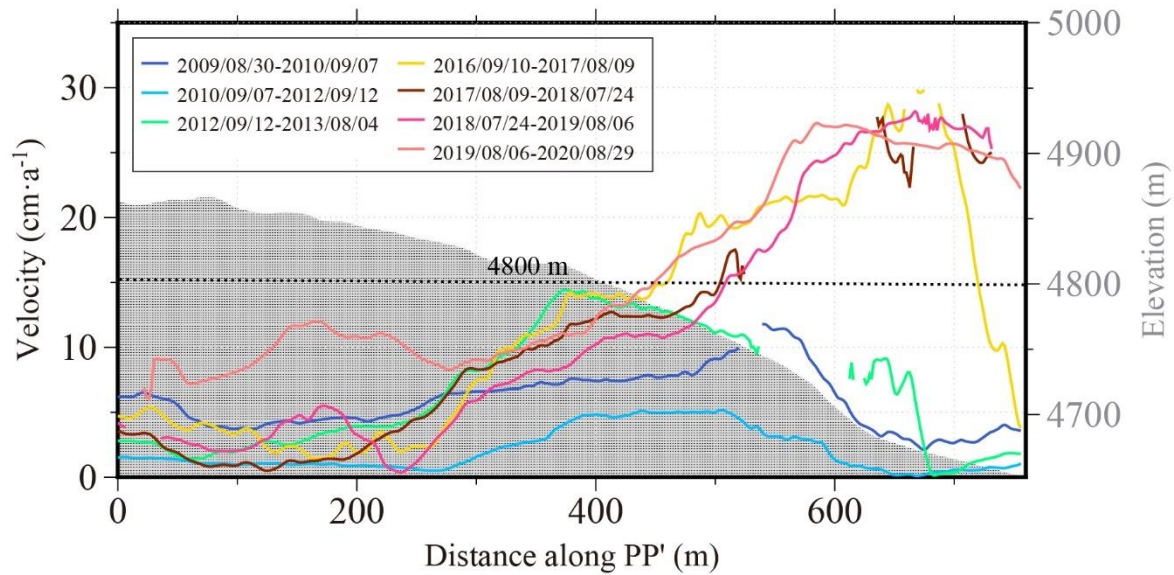


Figure 9: Surface velocities along the glacier central flow line PP' (see Fig. 8a) during the seven image correlation periods. The light-blue-shaded area indicates the surface topography (right axis) along the profile.

4.4 Hazard assessment for the glacier detachment

400 The KLP-37 glacier shares several similarities with the Aru Glacier. First, both exhibited continuous thinning in the source
region and thickening in the tongue region. Second, the ice flow directions along the two glaciers have both changed due to
the local topography. Also, both glaciers' widths gradually narrowed from the source region to the tongue, thus resulting in a
large amount of accumulated gravitational potential energy at the glacier front. We here assessed the runout hazard of two
endmember avalanche scenarios: (1) an avalanche starting from the crevasses in the accumulation region of KLP-37 by
405 assuming that the whole glacier detaches and (2) avalanche of the glacier tongue where apparent flow acceleration was
observed. Fig. 10a shows the ice thickness map of the two scenarios. The avalanche volumes for these two scenarios were
estimated to be about 27.06×10^6 and $6.63 \times 10^6 \text{ m}^3$, respectively.

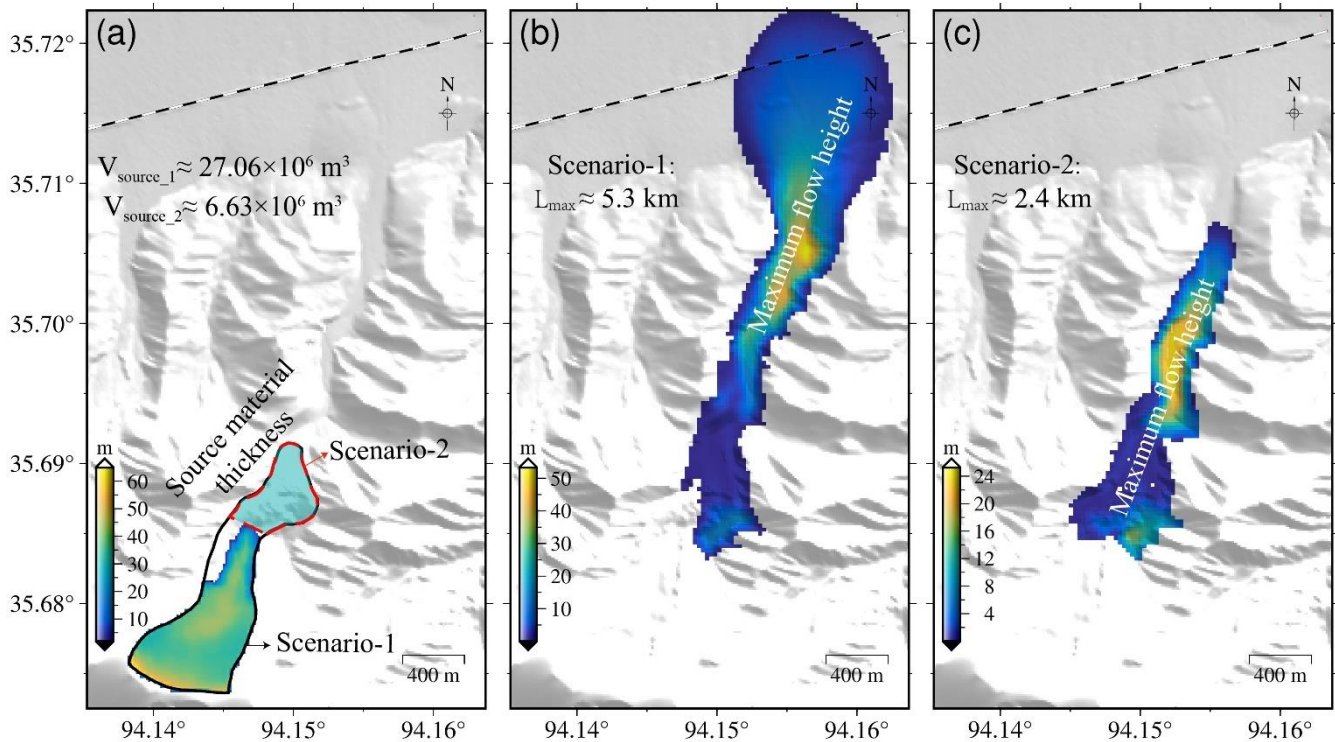


Figure 10: Runout extent estimates for the detachments of the whole glacier (scenario-1) and glacier tongue (scenario-2). (a) Ice (i.e., source material) thickness distribution of the avalanche scenarios-1 (black polygon) and scenario-2 (red polygon) derived from the global glacier ice thickness products of Farinotti et al. (2019). (b) The simulated maximum flow height of the avalanche for scenario-1 when choosing moderate friction values of 0.15 for Coulomb friction (μ) and $2500 \text{ m}\cdot\text{s}^{-2}$ for turbulent friction (ξ) in the Voellmy-Salm model. (c) The simulated results for scenario-2.

Given that the angle of reach (i.e., Fahrböschung) for low-angle glacier detachments mainly ranges between 5° and 10° , we roughly estimated the lower and upper bounds of possible runout distance for the two detachment scenarios. We assumed dropping elevations of about 950 m (5350-4400 m) and 500 m (4900-4400 m) for the two avalanche scenarios, respectively (see Fig. 10a). The estimated maximum runout distance is thus about 5.4~10.9 km for detachment of the whole glacier, and 2.8~5.7 km for the avalanche of the glacier tongue region. Considering that the Qinghai-Tibet railway is about 5.0 km from the scarp in the glacier source region, we can infer that the detachment of the whole glacier (i.e., scenario-1) will easily reach the railway. However, whether the detachment of the glacier tongue would influence the railway ($L > 4 \text{ km}$) depends on the value of Fahrböschung angle (i.e., $\arctan(H/L)$), and a hazardous influence is only anticipated when the Fahrböschung angle is smaller than 7° .

Figures 10b and 10c show the maximum accumulation flow height of the two avalanche models with moderate values of 0.15 and $2500 \text{ m}\cdot\text{s}^{-2}$ for μ and ξ , respectively. We found that the maximum flow heights are about 54 and 25 m for the avalanche

425 scenario-1 and scenario-2, respectively. The maximum runout distances of the two scenarios are about 5.3 and 2.4 km (Figs. 10b and 10c), which are smaller than these estimated from the angle of reach. The Fahrböschung values for the two avalanche scenarios were calculated to be both about 9° , laying in the range of $5^\circ\sim 10^\circ$ that was found on most detached glaciers. Similar to the assessment from the angle of reach, the VS modeling results also show that the avalanche whole glacier can easily threaten the railway. For the avalanche scenario-2, the ice material would not affect the railway due to the small avalanche
430 volume. However, considering that we cannot accurately determine the friction parameters, we will discuss how the variations of friction parameters would influence the runout distance estimate in Section 5.3.

5. Discussion

5.1 Classification of the landform

The landform we investigated lies in the front part of KLP-37 and shows a swallow body with a steep front. Field investigations
435 using ground-penetrating radar have shown that the lower permafrost altitude limit of the study region is about 4300 m, below the glacier terminus (Wu et al., 2005). Permafrost extent mapping also shows that the permafrost probability value over the glacier tongue region is 1 (Obu et al., 2019). These pieces of evidence indicate that the landform is located in a permafrost environment and raise concerns about whether it is an ice-cored moraine or rock glacier. Recent studies have documented accelerations of rock glaciers and slope failures at rock glacier fronts in the French and Italian Alps (Eriksen et al., 2018; Kofler et al., 2019; Marcer et al., 2020). We here argue that the landform is part of the KLP-37 glacier tongue from both geomorphic
440 and kinematic analyses below.

We first excluded the landform from the type of ice-cored moraine. Ice-cored moraines are generally formed by the isolation of a body of glacier ice through the establishment of a sediment/debris cover near the glacier margin, which shields the ice from melting (Lukas, 2011). The different melting rates between the protected sediment-covered ice and clean ice up glacier
445 then results in the sediment-covered ice body cutting off from the supply of active pure ice. Therefore, a typical ice-cored moraine should be disconnected from the active glacier ice margin. Regarding the landform at the front of KLP-37, however, the long-term advance of the glacier front without cutoff indicates that the inner body is connected with the glacier.

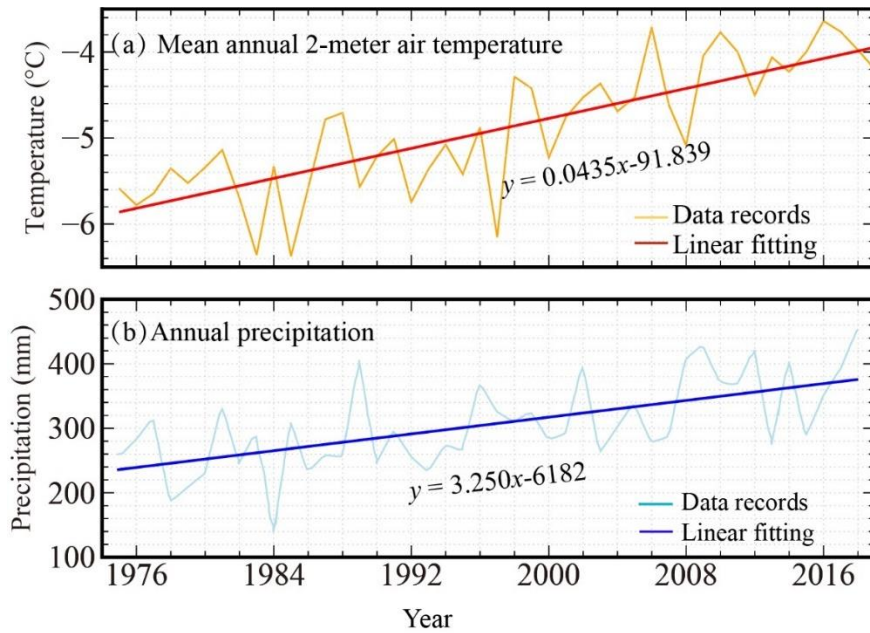
The KLP-37 glacier tongue differs from a rock glacier in both morphologic and kinematic patterns. First, rock glaciers are defined as landforms consisting of mixtures of unconsolidated rock debris and ice in an alpine environment. Debris cover on
450 a rock glacier is usually coarse, thick (>3 m), and the ice content is lower than 45% (Janke et al., 2015). The field photo in 2016 (Fig. 2c) showed that the debris cover on the KLP-37 glacier tongue was thin and uniform. The exposed clean ice in the photo also indicated the rich ice content of the landform. Second, we did not observe many ridges and furrows, the distinctive characteristics of rock glaciers, on the surface of the KLP-37 glacier front. In addition, rock glaciers typically move downslope at velocities smaller than $10\text{ m}\cdot\text{a}^{-1}$ (Kääb et al., 2021b; Wang et al., 2017), while the flow velocity of the landform from our
455 cross-correlation measurement reaches a maximum velocity of $\sim 30\text{ m}\cdot\text{a}^{-1}$. Therefore, we suggest that the landform of concern is part of the KLP-37 glacier tongue covered by a thin debris layer.

5.2 Mechanisms of the glacier dynamics

Multi-temporal satellite imagery revealed that the glacier tongue of KLP-37 advanced continuously between 1975 and 2021, and the snout advance velocity accelerated after 2015. From the analysis of changes in surface elevation and flow velocities, we suggest that the KLP-37 glacier tongue was undergoing a slow surge-like process during the observation period. We did not observe this process on the adjacent glaciers, indicating that the KLP-37 glacier has a unique glaciation setting causing the glacier tongue area to be highly active. Previous studies have shown that the factors resulting in glacier acceleration and even detachment mainly include the hydrothermal conditions of the glacier, topography, and the climate (precipitation/temperature) changes (Jacquemart et al., 2020; Kääb et al., 2021a; Kääb et al., 2018; Leinss et al., 2019). Next, we will discuss the possible mechanisms accounting for the dynamics of the KLP-37 glacier tongue.

The thermal regime of a glacier fundamentally influences its dynamics (Leinss et al., 2019). We cannot determine whether the ice/bed interface is temperate because no temperature measurements beneath the KLP-37 glacier are available. However, the long preservation of the ice-dammed lake aside from the glacier tongue suggests that the glacier front is probably frozen to the underlying bedrock. This is supported by field investigations and permafrost mapping showing that the glacier tongue lays in a permafrost environment (see Section 5.1). The cold thermal regime for parts of glacier and fronts has also been found at detached glaciers such as the Aru glacier, Leñas glacier, and Flat Creek glacier (Falaschi et al., 2019; Kääb et al., 2018; Jacquemart et al., 2020). The frozen base creates a favorable environment for ice accumulation and stress build-up, although it also increases the basal friction which is the threshold to be overcome for detachment occurrence. Detachment or acceleration of the glacier tongue occurs when the force balance cannot be achieved due to the increasing driving stress. The cross-correlations of the 2019–2020 image pair show that the mean velocities along the central profile were about 9.8 ± 1.4 and 22.3 ± 3.2 $\text{m} \cdot \text{a}^{-1}$ for regions above and below 4800 m, corresponding to flow velocities of 2.7 ± 0.4 and 6.1 ± 0.9 $\text{cm} \cdot \text{d}^{-1}$, respectively. These values are on the same order of magnitude as the estimated velocity of 2 $\text{cm} \cdot \text{d}^{-1}$ for pure ice deformation (Leinss et al., 2019; Round et al., 2017). We thus suggest that the internal ice creeping should mainly account for the downslope movement of KLP-37. However, given the fast and homogenous flow in the lower part of the glacier tongue, it is reasonable to postulate that basal sliding is at least partly responsible for the flow dynamics.

The KLP-37 glacier's geometry presumably plays an important role in accounting for the slow surge-like behavior of the glacier. From the high-resolution optical images (Fig. 3), we can observe that the flow direction of the glacier changes from $\text{NE}24^\circ$ to $\text{NE}5^\circ$ at an elevation of about 4800 m due to the local topography. The glacier tongue downslope of this turning exhibits a "V" shape (the upper part is wide, while the lower part is narrow). The specific shape of the glacier tongue results in the accumulation of large glacier masses at the place where the flow direction changes, thus increasing compressive pressure. The abrupt velocity increase between 2015 and 2016 could likely be the result of mass accumulation that happened further upstream in the previous years. Also, the slope angle is about $\sim 10^\circ$ above 4800 m but increases to $\sim 20^\circ$ at the lower place, making the lower part favorable for glacier acceleration. Compared with the glaciers nearby, the local topography at the KLP-37 front thus provides a preconditioning factor for the destabilization of the glacier tongue.



490

Figure 11: Mean annual 2-meter air temperature (a) and annual precipitation (b) at the Wudaoliang meteorological station (4613 m above sea level) about 60 km south of the KLP-37 glacier. The equations annotated represent the best linear fitting model of the data records.

495

The trend of a warmer and wetter climate in the past decades on the QTP may be the long-term driving factor for the continuous advance of the glacier tongue of KLP-37. Fig. 11 shows the mean annual 2-meter air temperature and mean annual precipitation at the Wudaoliang meteorological station about 60 km west (35.3°N, 93.6°E) to the glacier between 1975 and 2018. Both the air temperature and precipitation records show increasing trends: the increase rate of mean annual air temperature is $0.0435 \text{ } ^\circ\text{C}\cdot\text{a}^{-1}$, while the precipitation has an increasing rate of about $3.250 \text{ mm}\cdot\text{a}^{-1}$. Given the stepwise increase of snout advance velocity between 1975 and 2021 and the more than tripled mean flow velocity below 4800 m between 2009 and 2020 (Section 4), we suggest that the climate warming in the study region likely contributes to the long-term acceleration of the glacier tongue. The expansion of the ice-dammed lake in the past decade (Section 4.1) also justifies the study area's warming and wetting trend.

500

505

Previous studies have revealed that climate warming and increased rainfall can promote glacier movement and eventually lead to glacier detachments (Bai and He, 2020; Kääh et al., 2018; Tian et al., 2016). Taking the Aru glacier as an example, the regional climate warming was likely the reason for changing the glacier from retreat to slow advance in 2013 (a total advance of about 300 m before the ice avalanche in 2016) (Tian et al., 2016). Specifically, heavy precipitation accounting for 90% of the total precipitation of 2016 was recorded during the 40 days prior to the Aru glacier detachment, and the extreme precipitation was suggested to be the triggering factor for the detachment (Tian et al., 2016). The increase of meltwater in summer caused by climate warming could increase the overload of glacier surface and the supply of liquid water into the

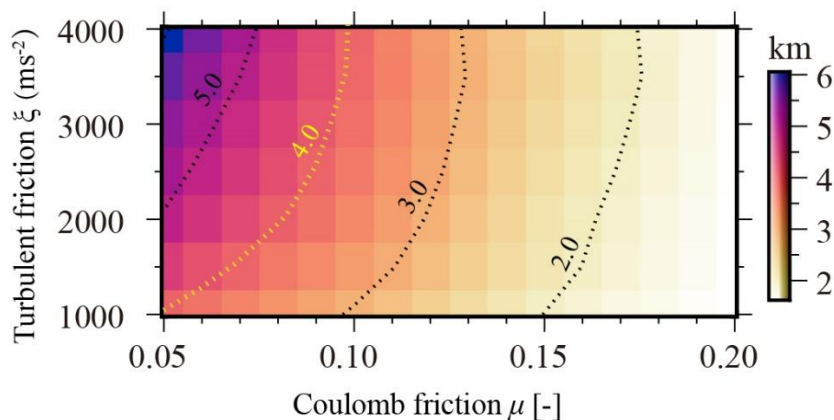
510 sliding surface, thus further promoting the downward movement of the glacier (Leinss et al., 2019).

In summary, we suggest that the cold glacier front, the particular local topography, and the long-term climate change in the East Kunlun Mountains are the main factors controlling the dynamics of the KLP-37 glacier tongue. With the warming and wetting trend of the regional climate, the risk of detachment of the KLP-37 glacier tongue may threaten the safety of the nearby Qinghai-Tibet railway and highway.

515 5.3 Limitations and implications for glacier detachment hazard assessment

Due to the limited documents of avalanching modeling for low-angle glacier detachments, we ran the VS model by specifying moderate friction parameters determined from the previous modeling of ice/rock avalanche events. Our modeling results show that the avalanche of the whole glacier would influence the Qinghai-Tibet railway, similar to the hazard assessment based on the angle of reach. The modeling results also show that the avalanche of the glacier tongue would not reach the railway.

520 However, it should be noted that the runout distance from VS modeling depends on the selection of friction parameters. To investigate how the altered frictional input parameters would influence the runout distance estimate of the avalanche scenario-2, we ran the VS model with multiple combinations of the parameter values. The result depicted in Fig. 12 shows that the runout distance would be longer with decreasing μ and increasing ξ . Only when μ is lower than 0.1, the avalanche of the KLP-37 glacier tongue would pose a threat to the Qinghai-Tibet railway (with a runout distance longer than 4 km). Note that
525 our modeling did not include the lubrication effects of fine-grained sediments under the glacier, which may reduce the avalanche friction and allow the detachments to accelerate particularly fast and cover long distances (Kääb et al., 2020). It is thus essential to monitor the dynamics of the KLP-37 glacier continually in combination with elaborate numerical simulation to predict its potential hazardous impacts.



530 **Figure 12: Variations of runout distance for varying friction parameters (μ and ξ) of the Voellmy-Salm model. The dotted lines represent the contour lines with the yellow one representing the runout distance (4 km) that will threaten the Qinghai-Tibet railway.**

Although plenty of glaciers in QTP have been retreating in the last several decades, glacier advancing has been ubiquitously observed either on surge-type glaciers or on those where ice-rock avalanches have occurred. Kääb et al. (2021a) suggested that glacier detachments could be seen as extreme endmembers of the range of surge-type and surge-like glacier instabilities, supported by the fact that some of glacier detachments exhibited surge-like advance ahead of the failures or occurred on surge-type glaciers themselves. In addition to this specific dynamic pattern, some communal geomorphic conditions have also been summarized from a compilation of 19 actual or possible glacier detachment events (Kääb et al., 2021a). The most frequent geomorphic characteristics on these detached glaciers are found to be the presence of abundant weak bedrocks/fine sediments under a glacier and gentle surface slope ranging between about 5° and 20°. As discussed in Section 5.2, both the dynamic and geomorphic patterns of the KLP-37 glacier align with these previously identified common conditions for a potential glacier detachment.

Our site-specific study of the KLP-37 glacier also adds the diversity of regional conditions for identifying avalanche-prone glaciers. First, we found that the specific shape of KLP-37 presumably plays a key role in influencing the dynamics of the glacier tongue. This indicates that the unique glacier geometry modulated by local topography should be considered in identifying and assessing glacier detachment hazards. Second, the KLP-37 glacier is located in a region where a few strong earthquakes have occurred in history (see Fig. 1 for the avalanches triggered by the 2001 earthquake). Given the triggering effect of large earthquakes on glacier detachment, particular attention should be paid to destabilized low-angle glaciers in active tectonic zones.

We have shown that using multi-source remote sensing images enables us to address the three-dimensional (i.e., horizontal and vertical) dynamics of a glacier, which is particularly helpful for identifying detachment-prone glaciers. In the future, monitoring techniques with short temporal sampling rates such as ground-based SAR and optical camera-based systems should be employed to capture the transient or accelerating signals of surface motion, which is vital for assessing glacier stability. Our simulations of the runout extent using avalanche modeling, combined with the empirical estimates of runout distance using the angle of reach, provide a preliminary assessment of the hazard influence of a potential glacier detachment. We highlight that such assessment should be valued in the future because it is mostly the only way to give first-hand information on the possible glacier detachment influence.

6. Conclusions

In this study, we analyzed the multi-decadal geomorphic changes of a small low-angle valley glacier KLP-37 in the East Kunlun Mountains with multi-source remote sensing imagery, followed by a hazard assessment of the glacier. We found that the glacier tongue has undergone slow surge-like processes in the past four decades. The glacier snout had been progressively advancing during the observation period, with a total advance of about 418 ± 24.13 m. The glacier surface exhibited continuous thinning in the source region and thickening in the tongue. Negative volume changes were found over the glacier tongue region, indicating continuous loss of the glacier mass there. We observed acceleration of the flow velocity over the glacier tongue,

565 with the mean velocity below 4800 m more than tripled, during the period 2009–2020.

Our observations suggest that several factors control the dynamics of the KLP-37 glacier. The change of flow direction of the glacier at an elevation of about 4800 m due to the local topography, coupled with the “V” shape of the glacier tongue geometry, presumably plays a crucial role for the surge-like behavior. The presence of an ice-dammed glacier lake and a supraglacial pond on the glacier tongue surface implies a hydrological influence on the glacier dynamics as well. Furthermore, the long-
570 term climate warming and increased annual precipitation likely enhance the glacier’s dynamic intensities, as manifested by the accelerations of snout advance and surface flow during the past decades.

The runout hazard assessments from both calculations based on the angle of reach (Fahrböschung) and Voellmy-Salm modeling suggest that the avalanche of the whole KLP-37 glacier would easily reach the Qinghai-Tibet railway. However, whether the detachment of the glacier tongue would threaten the safety of the railway depends on the selection of mobility index (“Fahrböschung”) or friction parameters. It is thus very essential to monitor the dynamics of the KLP-37 glacier continually
575 in the future to ensure the operation safety of the Qinghai-Tibet railway and highway downstream.

This study also demonstrates the possibility of using multiple remotely sensed data to investigate the multi-decadal geomorphic changes of glaciers in mountainous regions, where direct observations are scarce. Moreover, we have presented a means of evaluating a destabilized glacier's runout hazard based on remote sensing observations. The approach presented here for the
580 KLP-37 glacier can be easily adapted for other similar mountain glaciers in vast regions to assist in detachment hazard prevention and mitigation.

Code availability

The open-source ASP software for generating the ASTER DEM based on the ASTER stereo images is available at <https://ti.arc.nasa.gov/tech/asr/groups/intelligent-robotics/ngt/stereo/>. The HEXIMAP toolbox for extracting DEM from the
585 declassified Hexagon KH-9 satellite imagery can be downloaded at <https://github.com/gmorky/heximap>. The MASSFLOW software for conducting the glacier avalanche modeling is freely available at <http://www.massflow-software.com/> for an educational purpose.

Data availability

The SRTM-C and Hexagon KH-9 images are downloaded from the United States Geological Survey (USGS) EROS Archive.
590 The SRTM-X DEM and TanDEM are copyrighted and provided by the German Aerospace Center. The HMA DEMs are downloaded from NASA National Snow and Ice Data Center Distributed Active Archive Center. The ASTER stereo images are downloaded from the NASA Earthdata Search archive. The Planet images are freely downloaded from the Planet website (<https://www.planet.com/markets/education-and-research/>) for scientific research purposes.

Author contribution

595 XW collected the satellite data, did most of the result analyses, and wrote the draft. LL and YH helped revise the manuscript. QL helped interpret the results. RZ and BZ helped pre-process some of the satellite data. TW, LZ, and GL supported the field trip to the study site in 2016. All the authors were involved in the editing of the manuscript.

Competing interests

The authors declare that they have no conflict of interest.

600 Acknowledgements

The authors would like to thank the two anonymous reviewers for their constructive comments. This study is jointly supported by the National Natural Science Foundation of China (41804009 and 42071410), the National Key Research and Development Program of China (2017YFB0502700), the Project of Application Foundation of the Sichuan (China) Science and Technology (2020YJ0322, 2020JDTD0003), and The Hong Kong Research Grants Council (CUHK14303417 and CUHK14303119). Some
605 figures in this paper were plotted using the Generic Mapping Tools (Wessel et al., 2013).

References

- Allen, S.K., Schneider, D., and Owens, I.F.: First approaches towards modelling glacial hazards in the Mount Cook region of New Zealand's Southern Alps, *Natural Hazards and Earth System Sciences*, 9(2), 481–499, doi:10.5194/NHESS-9-481-2009, 2009.
- 610 Bai, X. and He, S.: Dynamic process of the massive Aru glacier collapse in Tibet, *Landslides*, 17(6), 1353–1361, doi:10.1007/s10346-019-01337-x, 2020.
- Bartelt, P., Salm, B., and Gruber, U.: Calculating dense-snow avalanche runout using a Voellmy-fluid model with active/passive longitudinal straining, *Journal of Glaciology*, 45(150), 242–254, doi:10.1017/S002214300000174X, 1999.
- 615 Bhabri, R., Watson, C.S., Hewitt, K., Haritashya, U.K., Kargel, J.S., Pratap Shahi, A., Chand, P., Kumar, A., Verma, A., and Govil, H.: The hazardous 2017–2019 surge and river damming by Shispare Glacier, Karakoram, *Sci Rep*, 10(1), 4685, doi:10.1038/s41598-020-61277-8, , 2020.
- Bolch, T., Piczonka, T., and Benn, D.I.: Multi-decadal mass loss of glaciers in the Everest area (Nepal Himalaya) derived from stereo imagery, *The Cryosphere*, 5(2), 349–358, doi:10.5194/tc-5-349-2011, 2011.
- 620 Chen, D., Xu, B., Yao, T., Guo, Z., Cui, P., Chen, F., and Zhang, R.: Assessment of past, present and future environmental changes on the Tibetan Plateau, *Chin Sci Bull*, 60: 3025–3035, doi:10.1360/N972014-01370, 2015. (In Chinese)
- Evans, S.G., Tutubalina, O.V., Drobyshev, V.N., Chernomorets, S.S., McDougall, S., Petrakov, D.A., and Hungr, O.: Catastrophic detachment and high-velocity long-runout flow of Kolka Glacier, Caucasus Mountains, Russia in 2002, *Geomorphology*, 105(3), 314–321, doi:10.1016/j.geomorph.2008.10.008, 2009.
- 625 Eriksen, H. Ø., Rouyet, L., Lauknes, T. R., Berthling, I., Isaksen, K., Hindberg, H., Larsen, Y., and Corner, G.D.: Recent Acceleration of a Rock Glacier Complex, Ádjet, Norway, Documented by 62 Years of Remote Sensing Observations. *Geophysical Research Letters*, 45(16), 8314–8323, doi: 10.1029/2018GL077605, 2018.
- Faillietaz, J., Funk, M., and Vincent, C.: Avalanching glacier instabilities: Review on processes and early warning perspectives, *Reviews of Geophysics*, 53(2), 203–224, doi:10.1002/2014rg000466, 2015.
- 630 Falaschi, D., Kääb, A., Paul, F., Tadono, T., Rivera, J.A., and Lenzano, L.E.: Brief communication: Collapse of 4Mm³ of ice from a cirque glacier in the Central Andes of Argentina, *The Cryosphere*, 13(3), 997–1004, doi:10.5194/tc-13-997-2019, 2019.

- Farr, T.G., Rosen, P.A., Caro, E., Crippen, R., Duren, R., Hensley, S., Kobrick, M., Paller, M., Rodriguez, E., Roth, L., Seal, D., Shaffer, S., Shimada, J., Umland, J., Werner, M., Oskin, M., Burbank, D., and Alsdorf, D.: The Shuttle Radar Topography Mission, *Reviews of Geophysics*, 45(2), 1–33, doi:10.1029/2005RG000183, 2007.
- 635 Gardelle, J., Berthier, E., Arnaud, Y., and Kääb, A.: Region-wide glacier mass balances over the Pamir-Karakoram-Himalaya during 1999–2011, *The Cryosphere*, 7(4), 1263–1286, doi:10.5194/tc-7-1263-2013, 2013.
- Gilbert, A., Leinss, S., Kargel, J., Kääb, A., Gascoïn, S., Leonard, G., Berthier, E., Karki, A., and Yao, T.: Mechanisms leading to the 2016 giant twin glacier collapses, Aru Range, Tibet, *The Cryosphere*, 12(9), 2883–2900, doi:10.5194/tc-12-2883-2018, 2018.
- 640 Guo, W., Liu, S., Xu, L., Wu, L., Shangguan, D., Yao, X., Wei, J., Bao, W., Yu, P., Liu, Q., and Jiang, Z.: The second Chinese glacier inventory: data, methods and results, *Journal of Glaciology*, 61, 357–372, doi: 10.3189/2015JG14J209, 2015.
- Haeberli, W., Huggel, C., Kääb, A., Zraggen-Oswald, S., Polkvoj, A., Galushkin, I., Zotikov, I., and Osokin, N.: The Kolka-Karmadon rock/ice slide of 20 September 2002: An extraordinary event of historical dimensions in North Ossetia, Russian Caucasus, *Journal of Glaciology*, 50(171), 533–546, doi:10.3189/172756504781829710, 2004.
- 645 Hall, D.K., Bayr, K.J., Schöner, W., Bindschadler, R.A., and Chien, J.Y.L.: Consideration of the errors inherent in mapping historical glacier positions in Austria from the ground and space (1893–2001), *Remote Sensing of Environment*, 86(4), 566–577, doi:10.1016/S0034-4257(03)00134-2, 2003.
- Hirano, A., Welch, R., Lang, H.: Mapping from ASTER stereo image data: DEM validation and accuracy assessment, *ISPRS Journal of Photogrammetry and Remote Sensing*, 57(5), 356–370, doi:10.1016/S0924-2716(02)00164-8, 2003.
- 650 Huggel, C., Zraggen-Oswald, S., Haeberli, W., and Kääb, A.: The 2002 rock/ice avalanche at Kolka/Karmadon, Russian Caucasus: assessment of extraordinary avalanche formation and mobility, and application of QuickBird satellite imagery, *Nature Hazard and Earth System Science*, 5, 173–187, doi:10.5194/nhess-5-173-2005, 2005.
- Huss, M. and Farinotti, D.: Distributed ice thickness and volume of all glaciers around the globe, *Journal of Geophysical research*, 117, F04010, doi:117 10.1029/2012JF002523, 2012.
- 655 Jacquemart, M., Loso, M., Leopold, M., Welty, E., Berthier, E., Hansen, J.S.S., Sykes, J., and Tiampo, K.: What drives large-scale glacier detachments? Insights from Flat Creek glacier, St. Elias Mountains, Alaska, *Geology*, 48(7), 703–707, doi:10.1130/g47211.1, 2020.
- Janke, J.R., Bellisario, A.C., and Ferrando, F. A.: Classification of debris-covered glaciers and rock glaciers in the Andes of central Chile, *Geomorphology*, 241, 98–121, doi:10.1016/j.geomorph.2015.03.034, 2015.
- 660 Jerome, V. D. W., Owen, L. A., Tapponnier, P., Xu, X., Kervyn, F., Finkel, R. C., and Barnard, P. L.: Giant, ~ M8 earthquake-triggered ice avalanches in the eastern Kunlun Shan, northern Tibet: Characteristics, nature and dynamics, *Geological Society of America Bulletin*, 116(3): 394–406. <https://doi/10.1130/B25317.1>, 2004.
- Kääb, A., Jacquemart, M., Gilbert, A., Leinss, S., Girod, L., Huggel, C., Falaschi, D., Ugalde, F., Petrakov, D., Chernomorets, S., Dokukin, M., Paul, F., Gascoïn, S., Berthier, E., and Kargel, J. S.: Sudden large-volume detachments of low-angle mountain glaciers – more frequent than thought?, *The Cryosphere*, 15, 1751–1785, doi:10.5194/tc-15-1751-2021, 2021a.
- 665 Kääb, A., Strozzì, T., Bolch, T., Caduff, R., Trefall, H., Stoffel, M., and Kokarev, A.: Inventory and changes of rock glacier creep speeds in Ile Alatau and Kungöy Ala-Too, northern Tien Shan, since the 1950s, *The Cryosphere*, 15, 927–949, doi:10.5194/tc-15-927-2021, 2021b.
- Kääb, A., Leinss, S., Gilbert, A., Bühler, Y., Gascoïn, S., Evans, S.G., Bartelt, P., Berthier, E., Brun, F., Chao, W.-A., Farinotti, D., Gimbert, F., Guo, W., Huggel, C., Kargel, J.S., Leonard, G.J., Tian, L., Treichler, D., and Yao, T.: Massive collapse of two glaciers in western Tibet in 2016 after surge-like instability, *Nature Geoscience*, 11(2), 114–120, doi:10.1038/s41561-017-0039-7, 2018.
- 670 Kofler, C., Mair, V., Gruber, S., Todisco, M. C., Nettleton, I., Steger, Zebisch M., Schneiderbauer S., and Comiti F.: When do rock glacier fronts fail? Insights from two case studies in South Tyrol (Italian Alps). *Earth Surface Processes and Landforms*, 1–17, doi:10.1002/esp.5099, 2021.
- 675

- Kotlyakov, V.M., Rototaeva, O.V., Nosenko, G.A.: The September 2002 Kolka Glacier catastrophe in North Ossetia, Russian Federation: evidence and analysis, *Mountain Research and Development*, 24(1): 78–83, doi:10.1659/0276-4741(2004)024[0078:Tskgci]2.0.Co;2, 2004.
- 680 Krieger, G., Moreira, A., Fiedler, H., Hajnsek, I., Werner, M., Younis, M., and Zink, M.: TanDEM-X: A Satellite formation for high-resolution SAR interferometry. *IEEE Transactions on Geoscience and Remote Sensing*, 45(11), 3317–3341, doi:10.1109/TGRS.2007.900693, 2007.
- Lasserre, C., Peltzer, G., Crampé, F., Klinger, Y., Van der Woerd, J., and Tapponnier, P.: Coseismic deformation of the 2001 Mw = 7.8 Kokoxili earthquake in Tibet, measured by synthetic aperture radar interferometry, *J. Geophys. Res.*, 110, B12408, doi:10.1029/2004JB003500, 2005.
- 685 Leinss, S., Willmann, C., and Hajnsek, I.: Glacier detachment hazard analysis in the West Kunlun Shan mountains. *IEEE International Geoscience and Remote Sensing Symposium (IGARSS) 2019*, Yokohama, Japan, pp. 4565–4568, doi:10.1109/IGARSS.2019.8900320, 2019.
- 690 Li, C., Jiang, L., Liu, L., and Wang, H.: Regional and altitude-dependent estimate of the SRTM C/X-band radar penetration difference on High Mountain Asia glaciers, *IEEE Journal of Selected Topics in Applied Earth Observations and Remote Sensing*, 14, 4244–4253, doi: 10.1109/JSTARS.2021.3070362, 2021.
- Li, J., Li, Z.W., Zhu, J.J., Li, X., Xu, B., Wang, Q.J., Huang, C.L., and Hu, J.: Early 21st century glacier thickness changes in the Central Tien Shan, *Remote Sensing of Environment*, 192, 12–29, doi:10.1016/j.rse.2017.02.003, 2017.
- Lukas, S.: Ice-cored moraines, In: Singh, V., Singh, P., and Haritashya, U.K. (Eds.), *Encyclopedia of Snow, Ice and Glaciers*. Springer, Heidelberg, 616-619, 2011.
- 695 Luo, J., Niu, F.J., Lin, Z.J., Liu, M.H., and Yin, G.A.: Variations in the northern permafrost boundary over the last four decades in the Xidatan region, Qinghai–Tibet Plateau, *Journal of Mountain Science*, 15(4), 765–778, doi:10.1007/s11629-017-4731-2, 2018.
- 700 Magnússon, E., Belart, J. M.-C., Pálsson, F., Ágústsson, H., and Crochet, P.: Geodetic mass balance record with rigorous uncertainty estimates deduced from aerial photographs and lidar data – Case study from Drangajökull ice cap, NW Iceland. *The Cryosphere*, 10(1), 159–177, doi: 10.5194/TC-10-159-2016, 2016.
- Maurer, J.M., Rupper, S.B., and Schaefer, J.M.: Quantifying ice loss in the eastern Himalayas since 1974 using declassified spy satellite imagery, *The Cryosphere*, 10(5), 2203–2215, doi:10.5194/TC-10-2203-2016, 2016.
- 705 Marcer, M., Nielsen, S. R., Ribeyre, C., Kummert, M., Duvillard, P., Schoeneich, P., Bodin X., and Genuite, K.: Investigating the slope failures at the Lou rock glacier front, French Alps. *Permafrost and Periglacial Processes*, 31(1), 15–30, doi:10.1002/ppp.2035, 2020.
- McNabb, R., Nuth, C., Käab, A., and Girod, L.: Sensitivity of glacier volume change estimation to DEM void interpolation, *The Cryosphere*, 13(3), 895–910, doi:10.5194/tc-13-895-2019, 2019.
- Nuth, C. and Käab, A.: Co-registration and bias corrections of satellite elevation data sets for quantifying glacier thickness change, *The Cryosphere*, 5(1), 271–290, doi:10.5194/tc-5-271-2011, 2011.
- 710 Obu, J., Westermann, S., Bartsch, A., Berdnikov, N. M., Christiansen, H. H., Dashtseren, A., and Kholodov, A.: Northern Hemisphere permafrost map based on TTOP modelling for 2000–2016 at 1 km² scale. *Earth-Science Reviews*, 193, 299–316, doi: 10.1016/J.EARSCIREV.2019.04.023, 2019.
- Ouyang, C., He, S., Xu, Q., Luo, Y., and Zhang, W.: A MacCormack-TVD finite difference method to simulate the mass flow in mountainous terrain with variable computational domain, *Computers & Geosciences*, 52, 1–10, doi:10.1016/j.cageo.2012.08.024, 2013.
- 715 Paul, F.: Repeat glacier collapses and surges in the Amney Machen Mountain Range, Tibet, possibly triggered by a developing rock-slope instability, *Remote Sensing*, 11(6), 708, doi:10.3390/rs11060708, 2019.
- Paul, F., Bolch, T., Briggs, K., Käab, A., McMillan, M., McNabb, R., and Strozzii, T. (2017). Error sources and guidelines for quality assessment of glacier area, elevation change, and velocity products derived from satellite data in the `Glaciers_cci`

- 720 project. *Remote Sensing of Environment*, 203, 256–275.
- Rashid, I., Majeed, U., Jan, A., and Glasser, N.F.: The January 2018 to September 2019 surge of Shisper Glacier, Pakistan, detected from remote sensing observations, *Geomorphology*, 351, 105394, doi:10.1016/j.geomorph.2019.106957, 2020.
- Riegler, G., Hennig, S.D., and Weber, M.: WORLDDDEM—a novel global foundation layer, *ISPRS International Archives of the Photogrammetry Remote Sensing and Spatial Information Sciences*, Munich, Germany, pp. 183–187, doi:10.5194/isprsarchives-xl-3-w2-183-2015, 2015.
- 725 Rosu, A.M., Pierrot-Deseilligny, M., Delorme, A., Binet, R., and Klinger, Y.: Measurement of ground displacement from optical satellite image correlation using the free open-source software MicMac, *ISPRS Journal of Photogrammetry and Remote Sensing*, 100, 48–59, doi:10.1016/j.isprsjprs.2014.03.002, 2015.
- Round, V., Leinss, S., Huss, M., Haemmig, C., and Hajnsek, I.: Surge dynamics and lake outbursts of Kyagar Glacier, Karakoram, *The Cryosphere*, 11, 723–739, doi: 10.5194/tc-11-723-2017, 2017.
- 730 Rupnik, E., Daakir, M., and Pierrot Deseilligny, M.: MicMac – a free, open-source solution for photogrammetry, *Open Geospatial Data, Software and Standards*, 2(1), 14. 10.1186/s40965-017-0027-2, 2017.
- Sakai, A.: Brief communication: Updated GAMDAM glacier inventory over high-mountain Asia, *The Cryosphere*, 13(7), 2043–2049, doi:10.5194/tc-13-2043-2019, 2019.
- 735 Scherler, D., Bookhagen, B., and Strecker, M.R.: Spatially variable response of Himalayan glaciers to climate change affected by debris cover, *Nature Geoscience*, 4(3), 156–159, doi:10.1038/ngeo1068, 2011.
- Shean D.: High Mountain Asia 8-meter DEMs derived from along-track optical imagery, NASA National Snow and Ice Data Center Distributed Active Archive Center, doi:10.5067/gsacb044m4pk, 2017.
- Shean, D., Alexandrov, O., Moratto, Z.M., Smith, B.E., Joughin, I.R., Porter, C., and Morin, P.: An automated, open-source pipeline for mass production of digital elevation models (DEMs) from very-high-resolution commercial stereo satellite imager, *ISPRS Journal of Photogrammetry and Remote Sensing*, 116, 101–117, doi:10.1016/j.isprsjprs.2016.03.012, 2016.
- 740 Tian, L., Yao, T., Gao, Y., Thompson, L., Mosley-Thompson, E., Muhammad, S., Zong, J., Wang, C., Jin, S., and Li, Z.: Two glaciers collapse in western Tibet, *Journal of Glaciology*, 63(237), 194–197, doi:10.1017/jog.2016.122, 2016.
- Wang, X., Liu, L., Zhao, L., Wu, T., Li, Z., and Liu, G.: Mapping and inventorying active rock glaciers in the northern Tien Shan of China using satellite SAR interferometry, *The Cryosphere*, 11, 997–1014, doi:10.5194/tc-11-997-2017, 2017.
- 745 Wang, X., Liu, Q., Zhang, B., Zhang, R., and Liu, G.: Monitoring and analyzing collapse of KLSK-37 glacier tongue in recent 40 years with multi-source remote sensing, *Geomatics and Information Science of Wuhan University*, 45(11), 1687–1696. doi: 10.13203/j.whugis20200214, 2020. (In Chinese)
- Wang, D. and Kääb, A.: Modeling glacier elevation change from DEM time series, *Remote Sensing*, 7(8), 10117–10142, doi: 10.3390/RS70810117, 2015.
- 750 Wessel, P., Smith, W.H.F., Scharroo, R., Luis, J., and Wobbe, F.: Generic Mapping Tools: improved version released, *Eos Trans. AGU*, 94(45): 409–410, doi:10.1002/2013EO450001, 2013.
- Wu, T., Li, S., Cheng, G., and Nan, Z.: Using ground-penetrating radar to detect permafrost degradation in the northern limit of permafrost on the Tibetan Plateau, *Cold Regions Science and Technology*, 41(3), 211–219 (In Chinese), doi:10.1016/j.coldregions.2004.10.006, 2005.
- 755 Wu, Y., Cui, Z., Liu, G., Ge, D., Yin, J., Xu, Q., and Pang, Q.: Quaternary geomorphological evolution of the Kunlun Pass area and uplift of the Qinghai-Xizang (Tibet) Plateau, *Geomorphology*, 36(3), 203–216, doi: 10.1016/S0169-555X(00)00057-X, 2001.
- Wu, X.H., Qian, F., and Pu, Q.Y.: Quaternary geology of the eastern Kunlun mountain, *Symposium of Geology on Tibetan Plateau*, pp. 1-18. Beijing: Geological Publishing House, 1982. (In Chinese)
- 760 Yasuda, T. and Furuya, M.: Dynamics of surge-type glaciers in West Kunlun Shan, Northwestern Tibet. *Journal of Geophysical Research: Earth Surface*, 120(11), 2393–2405, doi:10.1002/2015jf003511, 2015.